communications earth & environment

Supplementary Information for

Environmental impacts and carbon capture potential of ocean alkalinity enhancement

This PDF file includes:

Supplementary text
Figures S1 to S23
Tables S1 to S3
SI References

Supplementary Information Text

A stochastic model of marine particle cycling — IOTA

To explore the impacts of solid alkaline feedstocks on surface ocean particle dynamics, we developed a particle-based stochastic model of the marine biological pump. The core of the model are aggregates that are comprised of various primary particles (e.g., minerals, phytoplankton cells, dust particles). Our model calculates the physical characteristics of marine aggregates such as sinking rate, porosity, and size, and considers the impact of primary producer cell size, aggregation, temperature, dust flux, biomineralization, ballasting by mineral phases, oxygen, and the fractal geometry (porosity) of aggregates. The constitutive elements of our model, referred to here as "aggregates", are clusters of primary particles that emerge through interaction between phytoplankton cells (e.g., coccolithophorids, diatoms, picoplankton), various minerals (basalt, olivine, MgO, and CaO), and terrigenous dust (Fig. S1, Table S1). The model calculates the sinking rates and physical properties of many aggregates at each depth, with the distribution of primary particles (minerals, dust particles, picoplankton, coccolithophorids, diatoms, etc.) in each aggregate calculated according to the relative contribution flux of each primary particle to the total flux of material at each depth. The model is based on a previously published model that was aimed at reconstructing the geologic history of the ocean biological carbon pump and marine dissolved organic carbon (*1*-*3*).

The probability of aggregate formation as a result of a collision between two aggregates or primary particles i and j ($P_{i,j}$) is given by:

$$P_{i,j} = \gamma(z).\frac{\beta(i,j)}{\beta_{ref}}.\frac{NPP}{NPP_{ref}} \quad . \tag{1}$$

Here, β denotes the rate of collision between aggregates, while γ is an aggregation efficiency that varies with depth. The terms NPP, NPP_{ref}, and β_{ref}, denote marine net primary production (NPP) and reference values for NPP and collision rate, respectively. This formulation implies that in regions with high NPP, and thus elevated production of organic particles, aggregation probability will in general be higher. The aggregation efficiency parameter, γ, decreases with depth following Ref. (*4*). This assumption is based on observations in modern marine systems, in which the primary substrate that holds marine snow together in the water column is transparent exopolymer particles (TEP) — a mucus-like polysaccharide material exuded by phytoplankton and bacteria. Production of TEP tends to be highest under conditions of nutrient limitation during the senescent phase of phytoplankton blooms (*5*).

The collision rate (β) between particles i and j is governed by three primary encounter mechanisms: (1) Brownian motion; (2) fluid shear; and (3) differential settling (i.e., relatively larger and more rapidly settling particles sweeping up smaller particles). Mechanism (1) is the most common for very small particles, while mechanisms (2) and (3) dominate for larger particles. We follow previous work (*5*-*7*) in parameterizing the coagulation kernel β as the sum of collision frequency due to Brownian motion (β_{Br}), fluid shear (β_{sh}), and differential settling (β_{ds}):

$$\beta(i,j) = \beta_{Br} + \beta_{sh} + \beta_{ds} \tag{2}$$

Collision frequency due to Brownian motion, fluid shear, and differential settling, respectively, are parameterized according to:

$$\beta_{Br} = \frac{8kT}{6\mu}\frac{(r_i+r_j)^2}{r_i r_j} \quad , \tag{3}$$

$$\beta_{sh} = 9.8\frac{q^2}{1+2q^2}\sqrt{\left(\frac{\varepsilon}{\nu}\right)}\left(r_i + r_j\right)^3 \quad , \tag{4}$$

$$\beta_{ds} = \frac{1}{2}\pi\, MIN\left(r_i, r_j\right)^2\left|u_i - u_j\right| \quad . \tag{5}$$

Here k is the Stefan– Boltzman constant, T is temperature, μ is dynamic viscosity, ν is kinematic viscosity, and ε is the turbulent dissipation rate (set to 1×10^{-4}; Ref. (*5*)). The term q = MIN(r_i, r_j)/MAX(r_i, r_j), while r_i and r_j are the radii of the two aggregates/particles being evaluated for collision and u_i and u_j are the settling velocities of the two aggregates/particles.

The average probability of aggregation at each depth is then used to determine the proportion of particles that are incorporated into aggregates in the following depth. For instance, at the very top of the model domain where there is no aggregation, primary interacting particles (e.g., phytoplankton cells, synthetic minerals, dust, etc.) are evaluated for aggregation, and the average probability of aggregation at that depth is evaluated and used to determine the fraction of particles in the following depth will be contained within an aggregate.

1. Physical characteristics of aggregates

The volume of material in an aggregate is calculated as:

$$V_a = \alpha_1 V_C + \alpha_2 V_A + \alpha_3 V_{Di} + \alpha_4 V_{Pi} + \alpha_5 V_{Ca} + \alpha_6 V_{Feed} \quad , \tag{6}$$

where α is the number of primary particles in each aggregate, corrected for aggregate efficiency/probability of aggregation, and V is the volume of each primary particle, calculated using primary particle density and the total amount of material from each primary particle type (Table S1). The primary particle types include coccolithophorids (*C*), aragonite-producing phytoplankton (*A*), diatoms (*Di*), picoplankton (*Pi*), terrigenous dust (*D*), calcite (*Ca*), and anthropogenic alkaline feedstock (*Feed*).

An aggregate that forms through aggregation of smaller particles forms a fractal structure with a dimension, D_N, that describes its porosity ($p \sim {r_a}^{D_n}$, where p is the number of primary particles in the aggregate and r_a is the radius of the aggregate) (*8*). The closer D_N is to 3, the more the structure fills up three-dimensional space, thus lowering its overall porosity. The fractal dimension of marine snow has been inferred to be in the range of 1.3 to 2.3 from measurements of aggregate properties such as settling velocity, porosity, and size (*8, 9*). The aggregate radius, r_a, is then calculated using the fractal dimension and the radius of the primary particle, r_p:

$$r_a = r_p \cdot p^{1/D_n} \quad . \tag{7}$$

The radius of the primary particle, r_p, is calculated from its volume under the assumption that it is a sphere (*5*):

$$r_p = \sqrt[3]{\frac{3V_p}{4\pi}} \quad , \tag{8}$$

where the average volume of the primary particles in the aggregate (V_p), is calculated by dividing

the total volume of material in the aggregate, V_a, by the number of primary particles in each aggregate (p):

$$V_p = \frac{V_a}{p} \quad . \tag{9}$$

The aggregate porosity, φ, is related to the radius of individual particles that comprise the aggregate and the total radius of the aggregate:

$$\varphi = 1 - p\left(\frac{r_p}{r_a}\right)^3 \quad . \tag{10}$$

Aggregate density (ρ_a) is calculated using the composition-weighted density of the material in each aggregate (ρ_s), the density of seawater (ρ_{sw}), and aggregate porosity (φ):

$$\rho_a = (1-\varphi)\rho_s + \rho_{sw} \quad , \tag{11}$$

where ρ_s is calculated according to:

$$\rho_s = \frac{1}{p} \cdot [\alpha_1\rho_C + \alpha_2\rho_A + \alpha_3\rho_{Di} + \alpha_4\rho_{Pi} + \alpha_5\rho_D + \alpha_6\rho_{Ca} + \alpha_7\rho_{Feed}] \quad . \tag{12}$$

2. Particle sinking rates

Sinking rates of marine particles range from a few up to hundreds of meters per day (*10*), and have been found to increase with depth (*11*). In our model, the sinking rate of an aggregate is calculated using Stokes' law (*12*):

$$u = \sqrt{\frac{8r_a(\rho_a - \rho_{sw}).g}{3\rho_{sw}f(Re)}} \quad , \tag{13}$$

where g is acceleration due to gravity. The average sinking rate of aggregates at each depth can be calculated by dividing the sum of sinking rates of individual aggregates by the total number of aggregates at each depth. For low Reynolds numbers (Re), where viscous forces are dominant, the drag coefficient of an aggregate is calculated according to:

$$f(Re) = \frac{24}{Re} \quad , \tag{14}$$

$$Re = \frac{2r_a u}{\nu} \quad , \tag{15}$$

where ν is kinematic viscosity. For large Reynolds numbers, where turbulence starts to play an important role, the drag coefficient is calculated using Whites' approximation (*13*), which is valid for $Re < 2 \times 10^4$:

$$f(Re) = \frac{24}{Re} + \frac{6}{(1+\sqrt{Re})} + 0.4 \quad . \tag{16}$$

Substituting *f(Re)* with White's approximation results in a nonlinear equation that can be solved for u. Model aggregates are assumed to only sink vertically (i.e., there is no lateral current transport of aggregates). The applicable regime for estimating the drag coefficient for aggregates is calculated based on aggregate settling speed and size. Aggregates tend to reach high Re conditions when settling at a few hundred meters per day.

Within the salinity range of modern seawater, the viscosity of seawater is mainly a function of temperature (*14*). We use an expression that fits empirical data for seawater viscosity at 35 ppt to calculate the kinematic viscosity, ν, at temperature T[K] (*14*):

$$\nu = 5 \times 10^{-6}\, e^{\frac{2250}{T}} \quad . \tag{17}$$

Seawater temperature is assumed to be constant within the upper mixed layer and changes linearly within the thermocline, followed by a linear decrease below the thermocline to an end-member deep ocean temperature. This temperature structure mimics typical temperature-depth profiles in modern marine systems.

3. Zooplankton

Observations from the modern ocean suggest an important role for zooplankton in the marine particle cycle (*15, 16*). In particular, particle ingestion and fecal pellet production by zooplankton can represent an important vertical flux of organic carbon and other particle constituents, while evidence of slow-sinking oceanic aggregates in the modern deep ocean also suggests an important role of disaggregation/fragmentation of oceanic aggregates in the marine biological pump (*17*), much of which may be mediated by interaction with zooplankton. In any case, while the degree to which zooplankton influence the physical characteristics of the oceanic aggregates is not fully understood at present and the intensity of aggregate destruction by zooplankton likely varies by clade (*18*), experimental and modelling studies suggest that interaction between zooplankton and marine particles does occur and can lead to ingestion and fecal pellet production as well as fragmentation of aggregates.

The encounter rate of zooplankton with marine aggregates in the model is considered to be a function of marine net primary production.

$$E_{zoo} = \frac{NPP}{NPP_{ref}}\, z^{-b_{zoo}} \quad . \tag{18}$$

Where E_{zoo}, NPP, z, b_{zoo}, respectively, denote the encounter rate of zooplankton with marine aggregates, marine net primary production, depth, and coefficient for change in zooplankton abundance with depth. This parameterization for encounter rate of zooplankton with aggregates is largely consistent with the observation in the modern oceans where zooplankton biomass is found to be correlated with the strength of marine primary production (e.g., Ref. *19, 20*)). The value of b_{zoo} is chosen to be consistent with the observed depth profile of zooplankton biomass in the modern ocean (*19*). The value of E_{zoo} as expressed would be between 0 and 1, and for each aggregate at each depth the calculated encounter rate is compared to a randomly generated value, r. If $r < E_{zoo}$ the model evaluates a discrete zooplankton-aggregate interaction which can result in either ingestion or fragmentation of the aggregate.

Any discrete zooplankton-aggregate encounter event can lead to either ingestion or fragmentation. We assume that the probability of fragmentation is higher for larger particles, following Ref. *12* , and introduce a parameter R_{break} that increases with aggregate radius based on fragmentation experiments with tethered *Euphausia pacifica* (*5, 21*):

$$R_{break} = 0.1 \tan^{-1}\left[\frac{r_a}{10^4}\right] \quad , \tag{19}$$

where r_a is the aggregate radius, as described above. If a randomly generated value r is smaller than R_{break}, the aggregate fragments into a number of daughter particles. Following Ref. (*5*) we use a power law that describes the number of fragments (f) an aggregate can fragment into:

$$P_f = \sum_{i=2}^{f} 0.91.\, i^{-1.56} \quad . \tag{20}$$

The value for P_f is compared to a randomly generated value, r, for each successive f. When $r < P_f$, the number of fragments that the aggregate breaks into is obtained. The radius of the fragmented aggregate is then calculated by dividing the old radius by the number of fragments, ensuring mass conservation during fragmentation events.

Recent observations indicate that the efficiency of particle fragmentation by zooplankton varies as a function of water column depth, with elevated fragmentation in shallower parts of ocean mesopelagic zone and attenuated fragmentation in deeper waters (*17*). To account for variable efficiency of fragmentation, we re-scale R_{break} according to a dimensionless fragmentation efficiency (f_{frag}) defined as a power-law function of water column depth:

$$f_{frag} = k_{frag} \cdot z^{-0.258} \quad , \tag{21}$$

where k_{frag} is a scaling parameter and z is water column depth (*17*). Not all zooplankton taxa exhibit the same efficiency in fragmentating oceanic aggregates, and some groups will ingest oceanic aggregates and produce fecal pellets but will not generally fragment aggregates into smaller daughter particles (e.g., salps; (*18*)). We incorporate variation in efficiency of particle fragmentation and absence of fragmentation for some zooplankton by stochastically varying the value of k_{frag} between 0.1 and 1.

If the particle is not fragmented it is ingested and can produce fecal pellets. To assure that zooplankton only ingest aggregates of sufficient quality (e.g., with some non-trivial amount of organic matter), a randomly generated value, r, is compared to the organic weight fraction (f_{org}) in each aggregate and if $r < f_{org}$, the aggregate is considered appetitive and would become ingested. Ingestion of aggregates by zooplankton results in production of a range of faecal pellet sizes. Faecal pellets are treated by the model essentially as aggregates with much lower porosity (*22*) (Table S2). Fecal pellet sizes are computed in the model from the relationship between mean fecal pellet volume and prosome length for copepods (*23*):

$$\log PV = 2.58 \cdot \log PL - 2.38 \quad , \tag{22}$$

where PV and PL represent the fecal pellet volume and prosome length, respectively. To account for a range of sizes in different zooplankton classes (small/large), we sample stochastically from a uniform prior distribution of prosome lengths for each zooplankton size class (Table S2).

4. Rate of organic carbon degradation and efficiency of marine carbon pump

Our model employs a power-law formulation for organic matter degradation in the water column (*24, 25*). Degradation rates are a function of the amount and reactivity of organic matter, the latter of which is a function of organic matter age and the average sinking rate of aggregates. Specifically, the model uses the calculated average velocity of sinking aggregates from the particle model to calculate the age of organic particles in each depth layer (t_i):

$$t_i = \frac{z_i}{u_{i,average}} \quad , \tag{23}$$

where z_i is a given depth i and $u_{i,average}$ is the average settling velocity of aggregates at that depth. Subsequently, the organic matter content in aggregates can be calculated using an age-dependent power law for organic matter degradation rate at each depth i (R_i) (*24*):

$$R_i = -bt_i^{-a}C_i \quad , \tag{24}$$

where C_i is the concentration of organic matter at depth i and the constants a and b define the rate of organic carbon mineralization. This power law has been widely used to simulate the rate of organic matter degradation over various timescales, ranging from fresh phytoplankton to sedimentary organic matter with ages on the order of 10^6 years (*24*).

However, the standard power law formulation does not take into account the possible influence of temperature, dissolved oxygen concentrations, mineral matrix properties, or other factors that can potentially impact rates of carbon degradation (*26-28*). We modify the standard power law to include a temperature dependency (*29-31*) according to:

$$R_i = Q_{10}^{\frac{T_i - T_{ref}}{10}} . -bt_i^{-a}C_i \quad , \tag{25}$$

Where T_i is temperature at depth i, T_{ref} is a reference temperature, and Q_{10} is a standard temperature dependency factor, which for most biological systems is somewhere between 1.5-2.5 (*30, 31*).

5. Reaction-transport model

To explore the potential impact of alkaline mineral feedstocks on water column chemistry, we embed our stochastic particle model into a one-dimensional reaction transport model:

$$0 = \frac{d}{dz}\left[K_z \frac{d\,C_i}{dz} - C_i(z)v(z)\right] \pm R_i \quad . \tag{26}$$

Here z is depth below the photic zone, C_i represents concentration of dissolved tracer i, K_z is the turbulent diffusion coefficient, $v(z)$ is advection velocity, and R_i represents the rate(s) of reaction(s) that consume or produce a given dissolved tracer. Turbulent diffusion is assumed to be relatively vigorous above the chemocline in order to reflect the highly convective Ekman layer in the upper ocean, then decreases linearly to lower values in the thermocline to reflect the high impediment to vertical mixing caused by strong temperature stratification, and then increases linearly to higher values in the deep ocean where the absence of strong temperature gradients permits more effective vertical mixing. The advection coefficient is estimated by dividing the exchange flux between the high-latitude and deep ocean (~50 Sv; 1 Sv = 10^6 m^3/s) by the lateral (cross-sectional) area of the deep ocean. Due to uncertainty involved with this estimation, the advection term is multiplied by a fitting parameter, α, that can vary locally. Values for turbulent diffusion coefficients at the surface, thermocline, and the deep oceans along with the fitting parameter for advection were obtained through providing a rough fit against the measured DIC and oxygen depth profiles in a series of modern marine systems (*32*).

The rate of dissolved oxygen (O_2) consumption by aerobic respiration was simulated using a Michaelis-Menten formulation:

$$R_{resp} = R_C \frac{[O_2]}{K_i + [O_2]} \quad . \tag{27}$$

Here, K_i is the half-saturation constant for aerobic respiration, R_C is the carbon mineralization rate

as described above, and brackets denote concentration. The main source and sink for dissolved inorganic carbon (DIC) are the degradation of organic matter in the water column and precipitation of carbonate minerals, respectively. The rate of carbonate precipitation is assumed to be a function of carbonate saturation state:

$$R_{carb} = k_{carb}(\Omega - 1)^{1.7} \quad , \tag{28}$$

where:

$$\Omega = \frac{[Ca][CO_3^{2-}]}{K_{sp}} \quad . \tag{29}$$

Here k_{Carb}, Ω, $[Ca]$, $[CO_3^{2-}]$, and K_{sp}, correspond to the carbonate precipitation rate constant, the saturation index of carbonate, concentrations of dissolved calcium and carbonate ion, and carbonate precipitation equilibrium constant, respectively. The main chemical reactions that influence the concentration of total alkalinity (TA) in the water column include consumption of alkalinity through carbonate precipitation and its production through dissolution of the alkaline mineral feedstocks (basalt, olivine, MgO, and CaO). Boundary conditions used to solve the reaction-transport expressions for O_2, DIC, and TA were fixed-concentration at the top and the zero-gradient at the bottom of the model domain.

6. Model validation

To assess the ability of our particle model to capture the characteristics of particles and water column chemistry across a range of modern marine systems, we compare model results to commonly observed physical features of marine aggregates, to measured depth profiles of particulate organic carbon (POC), and to measured depth profiles of various chemical species relevant for the biological pump and the marine carbonate system (O_2, DIC, TA, and pH) in coastal and open ocean localities. Empirical observations of the sinking rates of marine aggregates yield a bimodal distribution, with peaks in particle sinking rate a ~1 m d^{-1} and above 500 m d^{-1}, suggesting that there are two major "classes" of marine aggregate with respect to particle sinking speeds (*33-36*). This complex bimodal behavior is reproduced well by our particle model (Fig. S2). Our model indicates a significant abundance of slow-sinking particles overall, consistent with measurements in modern subtropical waters in which more than 60% of total particulate organic carbon is found in particles with sinking rates less than 10 m d^{-1} (*33*).

While there is limited information at present on the distribution of porosity in marine aggregates, existing observations tend to suggest very high porosity for most marine aggregates, greater than ~0.9 and mostly approaching ~0.99 (*37-39*), except for fecal pellets which are compact and tend to have porosities around 0.45 – 0.65 (*22*). These observations are consistent with the porosities produced by our particle model (Fig. S3). The particle model is also capable of reproducing observations of particulate organic carbon (POC) content from neutrally buoyant sediment trap data (Fig. S4) and dissolved tracer concentrations across a range of coastal and open ocean settings (Fig. S5). Taken together, these results suggest that our particle model is capable of effectively representing the first-order dynamics of particle cycling, vertical carbon transport, and associated impacts on the marine alkalinity cycle across a range of marine environments.

7. Sensitivity analysis

Key parameters in our particle model were varied within the ranges specified in Table S2, and

changes in the average sinking rate of aggregates between maximum and minimum of each parameter were recorded. To be able to compare the effect of each parameter on the average sinking rate, the response of the model to change in input parameters were normalized (Fig. S6). The sign of the normalized effect indicate the directionality of the effect of each parameter on the average sinking rate, with positive normalized effect indicating that an increase in the parameter value would result in an increase in the average sinking rate (and vice-versa). Our results indicate, that calculated sinking rate is insensitive to most of the model input parameters such as flux of dust (F_{Dust}), mixing depth (L_{mix}), eddy diffusivity at surface (K_z), thermocline and deep ocean, turbulent dissipation rate (ε), and seawater surface temperature (*SST*). The parameters with the strongest influence on the sinking rate were the strength of marine net primary production (*NPP*), reference value for NPP (NPP_{ref}), aggregate fractal dimension, the fraction of NPP that is produced by various planktonic cells (e.g., picoplankton, aragonite forming phytoplankton), the coefficient for zooplankton encounter rate (b_{zoo}), and prosome length (*PL*) (Fig. S6).

Notably, by enhancing the encounter rate of zooplanktons with marine aggregates, our results show that an increase in the marine *NPP* or decrease in NPP_{ref} would result in higher rate of fecal production and production of a larger amount of compact fast-sinking fecal pellet. Our results also show that, since unlike picoplankton cells, coccolithophorid and aragonite forming phytoplankton have a reduced organic weight fraction, an increase in the contribution of coccolithophorid and aragonite forming phytoplankton to the marine NPP would result in a decrease in the organic fraction of marine aggregates, which in turn would decrease the rate of fecal pellet production by zooplankton.

8. Dissolution kinetics of alkaline feedstocks

Our model includes the physical properties and dissolution kinetics of four idealized alkaline mineral feedstocks: (1) crystalline basalt; (2) olivine (forsterite); (3) MgO (periclase); and (4) CaO (burnt lime). Crystalline basalt (CB) dissolution can be described as a sum of three parallel reactions dominated at acidic (*a*), neutral (*n*), and basic (*b*) conditions, respectively (*40*):

$$r_+^{\mathrm{CB}} = r_a^{\mathrm{CB}} + r_n^{\mathrm{CB}} + r_b^{\mathrm{CB}} \quad , \tag{30}$$

where r_+^{CB} represents the overall dissolution rate of crystalline basalt, and r_a^{CB}, r_n^{CB}, and r_b^{CB} denote dissolution rates for acidic, neutral, and basic mechanisms, respectively. In each case, the reaction rate is assumed to be related to the proton (H^+) activity in aqueous solution according to:

$$r_i^{\mathrm{CB}} = k_i^{\mathrm{CB}} a_{H^+}^{n_i^{\mathrm{CB}}} \quad , \tag{31}$$

where the subscript *i* refers to acidic, neutral, or basic mechanisms. The parameter k_i^{CB} is temperature-dependent rate constant, while a_{H^+} denotes the activity of aqueous H^+, and n_i^{CB} designates reaction order. Hydrogen ion activity is given as:

$$a_{H^+} = 10^{-\mathrm{pH}} \quad . \tag{32}$$

The temperature-dependent rate constant follows the form of an Arrhenius expression:

$$k_i^{\mathrm{CB}} = A_{0,i}^{\mathrm{CB}} e^{-\frac{E_{a,i}^{\mathrm{CB}}}{RT}} \quad , \tag{33}$$

where $A_{0,i}^{\mathrm{CB}}$ stands for a temperature independent pre-exponential factor, and $E_{a,i}^{\mathrm{CB}}$ denotes apparent activation energy for the reaction. Combining Eq. (30)-(33), the dissolution rate of crystalline basalt can be described by:

$$r_{+}^{\mathrm{CB}} = A_{0,a}^{\mathrm{CB}} e^{-\frac{E_{a,a}^{\mathrm{CB}}}{RT}} 10^{-n_a^{\mathrm{CB}}\mathrm{pH}} + A_{0,n}^{\mathrm{CB}} e^{-\frac{E_{a,n}^{\mathrm{CB}}}{RT}} 10^{-n_n^{\mathrm{CB}}\mathrm{pH}} + A_{0,b}^{\mathrm{CB}} e^{-\frac{E_{a,b}^{\mathrm{CB}}}{RT}} 10^{-n_b^{\mathrm{CB}}\mathrm{pH}} \quad . \tag{34}$$

The temperature independent pre-exponential factor, apparent activation energy, and reaction order for acidic, neutral, and basic conditions are fitted from experimental dissolution rates of crystalline basalts as a function of pH and temperature (*41*) (Table S3; Fig. S7). The dissolution kinetics of crystalline basalt derived from Eq. (34) achieve R^2 values of 0.9944 and 0.9405 for observational data obtained at 5°C and 25°C, respectively.

Empirical measurements of the dissolution rate of forsterite (*42-44*) suggest that overall olivine (Fo) dissolution can be described as a sum of two parallel reactions that dominate at acidic (*a*) and basic (*b*) conditions (*40, 45-49*):

$$r_{+}^{\mathrm{Fo}} = r_a^{\mathrm{Fo}} + r_b^{\mathrm{Fo}} \quad , \tag{35}$$

where r_i^{Fo} has the similar formulation as Eq. (31) with associated temperature-dependent rate constant (k_i^{Fo}) following the form of Arrhenius expression as in Eq. (33). The overall kinetic equation for calculating olivine dissolution rates combining the influence pH and temperature is given by:

$$r_{+}^{\mathrm{Fo}} = A_{0,a}^{\mathrm{Fo}} e^{-\frac{E_{a,a}^{\mathrm{Fo}}}{RT}} 10^{-n_a^{\mathrm{Fo}}\mathrm{pH}} + A_{0,b}^{\mathrm{Fo}} e^{-\frac{E_{a,b}^{\mathrm{Fo}}}{RT}} 10^{-n_b^{\mathrm{Fo}}\mathrm{pH}} \quad . \tag{36}$$

The parameters in Eq. (36) are derived by fitting experimental dissolution rates of forsterite (*42, 43, 50-53*) (Table S3; Fig. S8). The dissolution kinetics of forsterite olivine derived from Eq. (36) yields R^2 values exceeding 0.86 across a range of temperatures conditions (e.g., 0.9282 for data obtained at 25°C).

The overall dissolution of MgO can be formulated as a sum of two parallel reactions that dominate at under acidic (*a*) and neutral (*n*) conditions (*40, 45*):

$$r_{+}^{\mathrm{MgO}} = r_a^{\mathrm{MgO}} + r_n^{\mathrm{MgO}} \quad , \tag{37}$$

where the dissolution rates r_i^{MgO} regulated by acidic and neutral mechanisms are formulated similarly to Eq. (31) and the associated temperature-dependent rate constant (k_i^{Mgo}) is parameterized in an Arrhenius form as in Eq. (33). Thus, the overall expression for the dissolution kinetics of MgO is given by:

$$r_{+}^{\mathrm{MgO}} = A_{0,a}^{\mathrm{MgO}} e^{-\frac{E_{a,a}^{\mathrm{MgO}}}{RT}} 10^{-n_a^{\mathrm{MgO}}\mathrm{pH}} + A_{0,n}^{\mathrm{MgO}} e^{-\frac{E_{a,n}^{\mathrm{MgO}}}{RT}} 10^{-n_n^{\mathrm{MgO}}\mathrm{pH}} \quad . \tag{38}$$

The dissolution rates of MgO in solution are controlled by different surface complexation reactions as pH conditions change (*54*). Under acidic conditions (pH < 5), the reaction sequence during MgO dissolution is:

$$\mathrm{MgO_{surface}} + 2\mathrm{H^{+}_{solution}} \rightarrow \mathrm{MgO \cdot H^{+}_{surface}} \rightarrow \mathrm{Mg^{2+}} + \mathrm{OH^{-}_{solution}} \quad , \tag{39}$$

with the overall neutralization reaction described by:

$$MgO + 2H^+ \rightarrow Mg^{2+} + H_2O \quad . \tag{40}$$

Under these conditions, the rate-limiting step of the overall process is proton attack. At pH ≈ 5, MgO dissolution is limited instead by proton diffusion and the dissolution rate is dominated by proton concentration. Under neutral to alkaline conditions (pH > 7), the reaction sequence of MgO dissolution is:

$$MgOH^+_{surface} + OH^- \rightarrow MgOH^+ \cdot OH^-_{surface} \rightarrow Mg^{2+} + 2OH^-_{solution} \quad , \tag{41}$$

and the overall reaction is:

$$MgO + H_2O \rightarrow Mg^{2+} + 2OH^+ \quad . \tag{42}$$

Under these conditions, the rate-limiting step is OH^- ion attack (which drives discharge of the $MgOH^+$ from the solid surface), followed by the desorption of Mg^{2+} and OH^-. The first step in Eq. (41) is essentially a hydroxylation reaction that results in the formation of brucite ($Mg(OH)_2$):

$$MgO + H_2O \rightarrow Mg(OH)_2 \quad . \tag{43}$$

Scanning electron microscopy reveals the formation of a hydroxylated layer of $Mg(OH)_2$ crystals at the surface of MgO during dissolution (*54*). Since the hydration reaction of MgO is rapid (*54, 55*), MgO dissolution is ultimately rate-limited by $Mg(OH)_2$ dissolution when pH is greater than 7. Similar reactivity of MgO and $Mg(OH)_2$ at neutral to alkaline conditions (*56*) is also implied by the convergence of dissolution rates for MgO and $Mg(OH)_2$ at pH range from 6 to 10 (*54, 57*) (Fig. S9). Considering the scarcity of dissolution rate data for MgO at a pH range between 6 to 10, we estimate the values for parameters in Eq. (38) using experimental dissolution rate data for brucite as a function of pH at a temperature of 25°C (*57*) (Table S3). The kinetic regression generated by Eq. (38) achieves an R^2 value of 0.9218 for dissolution rate data at 25°C.

There is very limited experimental data for dissolution rates of CaO (burnt lime) as a function of pH and temperature (*58-60*). In our model, dissolution of CaO is described as a one-term reaction that is assumed valid for all pH conditions:

$$r_+^{CaO} = k^{CaO} a_{H^+}^{n^{CaO}} \quad , \tag{44}$$

where k^{CaO} is temperature-dependent rate constant, a_{H^+} is the activity of aqueous H^+, and n^{CaO} denotes reaction order. With k^{CaO} being again formulated in the form of an Arrhenius expression as in Eq. (33), the overall expression for CaO dissolution is given by:

$$r_+^{CaO} = A_0^{CaO} e^{-\frac{E_a^{CaO}}{RT}} 10^{-n^{CaO}pH} \quad . \tag{45}$$

Similar to MgO, the first step of CaO dissolution under neutral to alkaline conditions is the rapid conversion through hydroxylation to $Ca(OH)_2$ ("slaked lime" or portlandite) (*61-63*):

$$CaO + H_2O \rightarrow Ca(OH)_2 \quad . \tag{46}$$

It should thus be viable to approximate CaO dissolution kinetics using $Ca(OH)_2$ dissolution rates, under the assumption that the surface hydroxylation reaction will not be rate-limiting. We estimate the values for the temperature independent pre-exponential factor, apparent activation energy, and

reaction order in Eq. (45) through the fitting of experimental dissolution rates for $Ca(OH)_2$ as a function of pH and temperature (*59*) (Table S3; Fig. S10). The kinetic regression generated by Eq. (45) yields an R^2 value of 0.8993 for dissolution rate data obtained at 51°C, although we are unable to evaluate the goodness-of-fit for data obtained at 25°C because available dissolution rates are measured at a single pH value (Fig. S10).

9. Treatment of particle size for alkaline mineral feedstocks

Previous work on ocean-based enhanced weathering has ignored differences in particle size within the reacting particle pool, and instead assumes that reacting feedstock grains sink as perfect spheres with a single uniform spherical diameter (e.g., Ref. (*64*)). However, mechanical comminution generally produces an approximately log-normal distribution of feedstock particle sizes (*65*), whose modal size and dispersion will depend on initial feedstock and grinding/milling technology (*66, 67*). Our default model builds from recent work on enhanced silicate weathering in agricultural systems and other terrestrial settings (*67, 68*), employing a particle size distribution (PSD) rather than a single feedstock particle size. By default our feedstock PSD is that of Ref. (*68*), discretized into the size-mass fraction bins shown in Fig. S11.

It is important to note that feedstock PSD is likely to be variable across different feedstock types, and an important topic for future research is evaluating likely PSD characteristics for different potential feedstocks along with the process CO_2 penalties and energetic demands of their production. The PSD characteristics of natural feedstocks in particular (e.g., basalt and olivine) are likely to vary substantially even within a single feedstock type (*69*), and the physical characteristics of synthetic alkaline metal oxide feedstocks are potentially very different from those of natural silicate mineral feedstocks. However, we consider this uncertainty very unlikely to impact our primary conclusions for a number of reasons. First, empirical observations suggest that our PSD contains a relatively large number of small, rapidly reacting particles compared to that typical of currently available natural silicate mineral feedstocks (*68-70*). As a result, our default model minimizes the deleterious impacts of basalt and olivine feedstocks on particle composition and zooplankton abundance while maximizing potential alkalinity production. Second, the reaction kinetics of CaO are so rapid that complete or near-complete dissolution in very shallow waters is extremely likely almost regardless of assumed feedstock particle size (Fig. S11). In addition, it is possible that synthetic feedstocks could be engineered to have significantly different (and more reactive) particle characteristics than natural mineral substrates, depending on the feedstock production process. Jet milling of portland cement and limestone mixtures, for instance, can produce a narrow range of very small (~4 μm) particles (*71*), something unlikely to be achieved for natural feedstocks without prohibitive energetic penalties. As noted in the main text, the lone exception to this amongst the feedstocks explored here is MgO. Under some combinations of NPP, feedstock application rate, and feedstock PSD characteristics, our model predicts that MgO will basically behave similarly to CaO — yielding near complete dissolution in shallow waters with efficient alkalinity release and minimal impact on particle composition and zooplankton abundance (Fig. S12-S16). However, at larger grain sizes (or lower ratios between NPP and feedstock application rate) MgO begins to noticeably impact marine particle dynamics.

10. Earth system modelling of ocean alkalinity enhancement

Here we explore the impacts of large-scale ocean alkalinity enhancement using solid alkalinity

sources with a 'carbon-centric' version of the Grid ENabled Integrated Earth system model — cGENIE (*72, 73*). The ocean physics and climate model components of cGENIE comprise a reduced physics (frictional geostrophic) 3-D ocean circulation model coupled to a 2-D energy-moisture balance model (EMBM) and a dynamic-thermodynamic sea ice model (*74, 75*). Heat, salinity, and biogeochemical tracers are transported via parameterized isoneutral diffusion and eddy-induced advection (*74-76*). The ocean model exchanges heat and moisture with the atmosphere, sea ice, and land while being forced at the ocean surface by zonal and meridional wind stress according to a specified static wind field. Heat and moisture are horizontally mixed throughout the atmosphere and exchange heat and moisture with the ocean and land surfaces, with precipitation occurring above a given relative humidity threshold. The sea ice model tracks horizontal ice transport and exchanges of heat and fresh water, using the thickness, areal fraction, and concentration of ice as prognostic variables. Full descriptions of the climate model and ocean physics can be found in Refs. *74* and *75*. The ocean model is configured here as a 36 x 36 equal-area grid (uniform in longitude and sine of latitude) with 16 logarithmically spaced depth levels and seasonal forcing at the ocean surface.

The ocean biogeochemistry module in cGENIE controls air-sea gas exchange and the transformation and repartitioning of biogeochemical tracers within the ocean. The ocean biological carbon pump is driven by a parameterized uptake rate of nutrients in the surface ocean, with this flux converted stoichiometrically to biomass that is then partitioned into particulate or dissolved organic matter for downstream advective transport, sinking, and remineralization within the ocean interior. Dissolved organic matter is transported with the ocean circulation and decays according to a specified time constant, while particulate organic matter is instantaneously exported from the surface ocean and is remineralized within the ocean interior following an exponential decay function with a specified remineralization length scale. The ocean biogeochemistry also contains a fully coupled carbonate system, which tracks individual dissolved inorganic carbon (DIC) species, dissolved alkalinity, and ocean pH. Calcium carbonate forms in surface ocean grid cells at a stoichiometric ratio with organic matter production and is dissolved in the ocean interior or shallow marine sediments depending on ambient temperature, pressure, and carbonate chemistry (*77*). Detailed description and validation of biogeochemistry in cGENIE is provided in (*73, 78*).

The model climate system and carbonate cycle are spun up as a closed system for 20 kyr with atmospheric abundances of CO_2, CH_4, and N_2O imposed at preindustrial values in order to bring the ocean-atmosphere system and shallow sediments into steady state. All subsequent simulations are branched from the spinup at model year 1765, and run to year 2300 according to the Representative Concentration Pathway (RCP) and Extended Concentration Pathway (ECP) scenarios for atmospheric CO_2, CH_4, and N_2O (*79*). Time-varying atmospheric abundances of CH_4 and N_2O are imposed according to a given RCP/ECP trajectory for all simulations, while atmospheric CO_2 abundance is emission-driven. The emission trajectory for a given RCP is first computed by the model by prescribing the atmospheric CO_2 trajectory for that scenario, with all subsequent runs utilizing the emission trajectory diagnosed in cGENIE for each RCP/ECP pathway. Concentration-driven and inverted emission-driven atmospheric compositions are shown in Fig. S17. Temperature trajectories are compared to CMIP5 results in Fig. S18 for the moderate-emissions (RCP4.5) and high-emissions (RCP8.5) pathways, while surface ocean carbonate system parameters are compared to gridded observational data in Fig. S19.

We use IOTA to compute the depth-integrated alkalinity release during CaO dissolution within the upper 80m of a coastal marine water column at three different application rates referred to here

as "low" (100 g m^{-2} y^{-1}), "moderate" (300 g m^{-2} y^{-1}), and "high" (500 g m^{-2} y^{-1}) application scenarios. This depth range corresponds to the upper grid cell resolution in the cGENIE ocean model but is also a reasonable annually averaged value for much of the global ocean (*80*). The computed alkalinity fluxes are introduced as dissolved tracer fluxes into surface ocean grid cells (e.g., as dissolved Ca^{2+} and alkalinity) starting at year 2030 according to two different idealized deployment scenarios (Fig. S20). In the first, alkalinity enhancement is deployed exclusively along coastlines within 60ºN/S, while in the second the same overall mass flux is spread across regions of relatively high background sea-air gas exchange fluxes of CO_2. Results from the 'coastal' scenario are discussed in the Main Text, while results from the 'degas' scenario are shown in Fig. S21-S22.

A full techno-economic assessment across a range of deployment strategies will ultimately be required to establish plausible feedstock application rates for this carbon management approach. However, we can estimate the overall mass fluxes implied by our deployment scenarios by combining the area-normalized feedstock flues implemented in our particle model with the deployment areas in the two idealized scenarios (which are set equal by design). Results of deployment scenarios are shown in Fig. S23. The overall mass (feedstock) fluxes implied by our low, moderate, and high application scenarios are 6.2, 18.6, and 31.1 Gt of feedstock per year, respectively. This corresponds respectively to 10.3, 31.0, and 51.8% of current (2020) raw mineral (non-metallic) and ore use (*81*), and to 5.6, 16.9, and 28.3% of estimated raw mineral and ore use in 2060 (*82*). For comparison, current global cement production is ~4 Gt y^{-1} (*83*) and has been projected to roughly double by 2100 (*84, 85*), while global available carbonate mineral deposits shallower than 25m and within 50 km of coastlines amount to ~570 Gt y^{-1} of raw feedstock potential if deployed between 2030-2100 (*86*).

548 **Table S1.** The probability, *P*, for a type of particle to be produced and range of values for different
549 conditions, different types of primary particles with the amount of material in each particle (pmol
550 particle^{-1}) and their densities. Particle types: C is coccolithophorid, A is Aragonite forming
551 phytoplankton, Di is diatom, Pi is picoplankton, D = dust, Ca is calcite.

Type	*P*	Range	OrgC	Calcite	Aragonite	bSi	Clay	ρ (g cm^{-3})
C	0.06	0-0.25	7	1.5	0	0	0	1.92
A	0.06	0-0.25	7	0	1.5	0	0	1.92
Di	0.02	0-0.15	15	0	0	5	0	1.24
Pi	0.7	0.3-0.9	1	0	0	0	0	1.06
D	0.15	0.05-0.2	0	0	0	0	2.85	2.65
Ca	0.01	0-0.05	0	2.5	0	0	0	2.55

552
553
554
555
556
557
558
559
560
561
562
563
564
565
566
567
568
569
570
571
572
573
574
575
576
577
578
579
580
581
582
583
584
585

Table S2. Default parameters for stochastic model of sinking rates of aggregates and parameter ranges used in sensitivity analysis (SA).

Parameter	Symbol	Value	Unit	Range used in the SA
Net primary production flux	NPP	1000	gC m^{-2} yr^{-1}	100-1000 (*87*)
Reference net primary production flux	NPP_{ref}	1000	gC m^{-2} yr^{-1}	500 & 1000
Dust flux	F_{Dust}	2	g m^{-2} yr^{-1}	1-10 (*88*)
Calcite flux	F_{Ca}	0.01	Pg yr^{-1}	0.005-0.05
Silica flux	F_{silica}	0.005	Pg yr^{-1}	0.001-0.01
Mixing depth	L_{mix}	50	m	50-100
Temperature dependency factor	Q_{10}	1	-	1.2-2.2 (*30, 31*)
Depth scale for thermocline	L_{thermo}	80	m	80-100
Reference temperature	T_{ref}	4	° C	4-25
Aggregation efficiency factor	K_{aggr}	0.5	-	0.1-1
Fractal dimension	D_N	2	-	1.3-3 (*5*)
Seawater surface temperature	SST	25	° C	20-28
Seawater surface density	SSD	1.0255	g/cm^3	1.0253-1.026
Fraction of NPP by picoplankton	f_{Pi}	0.4	-	0.4 - 0.9
Fraction of NPP by coccolithophorid	f_C	0.3	-	0.1 – 0.3
Fraction of NPP by Aragonite forming phytoplankton	f_A	0.3	-	0.1 – 0.3
Fraction of NPP by diatom	f_{Di}	0	-	0 – 0.1
Stefan– Boltzman constant	k_{Boltz}	1.380×10^{-23}	m^2 kg s^{-2} K^{-1}	
Reference value for collision rate	β_{ref}	1×10^{-15}	m^3/s	1×10^{-15}- 1×10^{-12}
Turbulent dissipation rate	ε	1×10^{-4}	m^2/s^3	1×10^{-5} - 1×10^{-3} (*5*)
Prosome Length (small zooplankton)	PL	-	µm	100-500 (*23*)
Prosome Length (large zooplankton)	PL	-	µm	300-2000 (*23*)
Zooplankton abundance coefficient	b_{zoo}	0.5	-	0.2-0.5
Fecal pellet porosity	Φ_{fecal}	-	-	0.5-0.6 (*37-39*)
Eddy diffusion coefficient at the surface	$K_{z,\ surf}$	5×10^{-3}	m^2/s	10^{-3} - 10^{-2} (*89*)
Eddy diffusion coefficient at the thermocline	$K_{z,\ therm}$	6×10^{-4}	m^2/s	10^{-4} - 10^{-3} (*89*)
Eddy diffusion coefficient in the deep ocean	$K_{z,\ depp}$	6×10^{-3}	m^2/s	10^{-3} - 10^{-2} (*89*)
Monod constant for O_2	K_i	2	μM	1 – 2 (*90*)
Iron oxidation rate constant	k_{fe}	100	1/µM/year	100-500 (*90*)
Calcium concentration	$[Ca]$	10	mM	-

590 **Table S3.** Summary of rate parameters used in Eqs. (34), (36), (38), and (45) to estimate area-
591 normalized dissolution rates of crystalline basalt, olivine (forsterite), MgO, and CaO, respectively,
592 as a function of pH and temperature.

Parameter	Symbol	Value	Unit	Source
Crystalline basalt				
temperature independent pre-exponential factor (acid)	$A_{0,a}^{\mathrm{CB}}$	$10^{-1.76}$	mol m^{-2} s^{-1}	this study
temperature independent pre-exponential factor (neutral)	$A_{0,n}^{\mathrm{CB}}$	$10^{-6.26}$	mol m^{-2} s^{-1}	this study
temperature independent pre-exponential factor (basic)	$A_{0,b}^{\mathrm{CB}}$	$10^{-2.41}$	mol m^{-2} s^{-1}	this study
apparent activation energy (acid)	$E_{a,a}^{\mathrm{CB}}$	32	kJ mol^{-1}	this study
apparent activation energy (neutral)	$E_{a,n}^{\mathrm{CB}}$	30	kJ mol^{-1}	this study
apparent activation energy (basic)	$E_{a,b}^{\mathrm{CB}}$	30	kJ mol^{-1}	this study
reaction order (acid)	n_a^{CB}	0.8	—	this study
reaction order (neutral)	n_n^{CB}	0.0	—	this study
reaction order (basic)	n_b^{CB}	0.7	—	this study
Olivine (forsterite)				
temperature independent pre-exponential factor (acid)	$A_{0,a}^{\mathrm{Fo}}$	$10^{5.17}$	mol m^{-2} s^{-1}	this study
temperature independent pre-exponential factor (basic)	$A_{0,b}^{\mathrm{Fo}}$	$10^{2.35}$	mol m^{-2} s^{-1}	this study
apparent activation energy (acid)	$E_{a,a}^{\mathrm{Fo}}$	70.4	kJ mol^{-1}	(*49*)
apparent activation energy (basic)	$E_{a,b}^{\mathrm{Fo}}$	60.9	kJ mol^{-1}	(*49*)
reaction order (acid)	n_a^{Fo}	0.46	—	(*47*)
reaction order (basic)	n_b^{Fo}	0.256	—	(*47*)
MgO				
temperature independent pre-exponential factor (acid)	$A_{0,a}^{\mathrm{MgO}}$	$10^{3.57}$	mol m^{-2} s^{-1}	this study
temperature independent pre-exponential factor (neutral)	$A_{0,n}^{\mathrm{MgO}}$	$10^{-0.77}$	mol m^{-2} s^{-1}	this study
apparent activation energy (acid)	$E_{a,a}^{\mathrm{MgO}}$	59	kJ mol^{-1}	(*40*)
apparent activation energy (neutral)	$E_{a,n}^{\mathrm{MgO}}$	42	kJ mol^{-1}	(*40*)
reaction order (acid)	n_a^{MgO}	0.115	—	this study
reaction order (neutral)	n_n^{MgO}	0	—	this study
CaO				
temperature independent pre-exponential factor	A_0^{CaO}	$10^{-0.72}$	mol m^{-2} s^{-1}	this study
apparent activation energy	E_a^{CaO}	13.7	kJ mol^{-1}	(*91*)
reaction order	n^{CaO}	0.04	—	this study

593
594
595
596
597
598
599
600
601
602
603
604
605

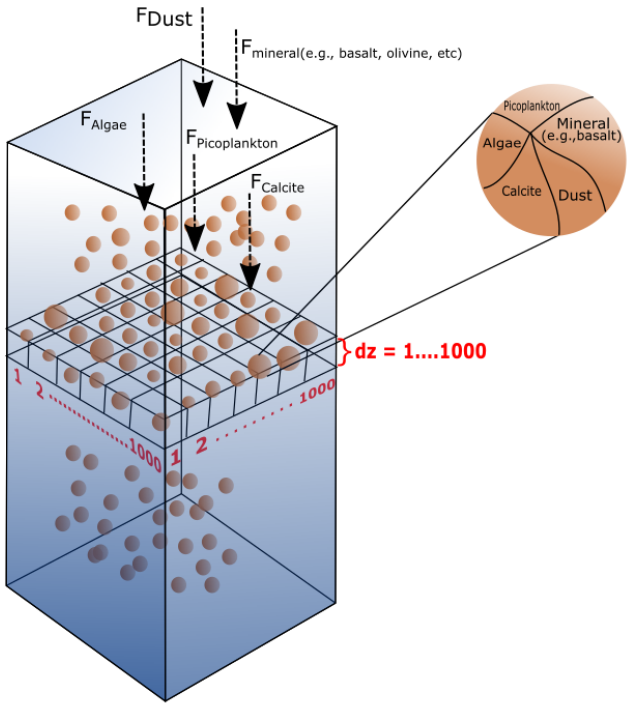

Fig. S1. Schematic presentation of the stochastic particle model. Fluxes (F_i) include picoplankton, algae, dust, calcite, and mineral feedstocks (e.g., basalt, olivine, MgO, CaO).

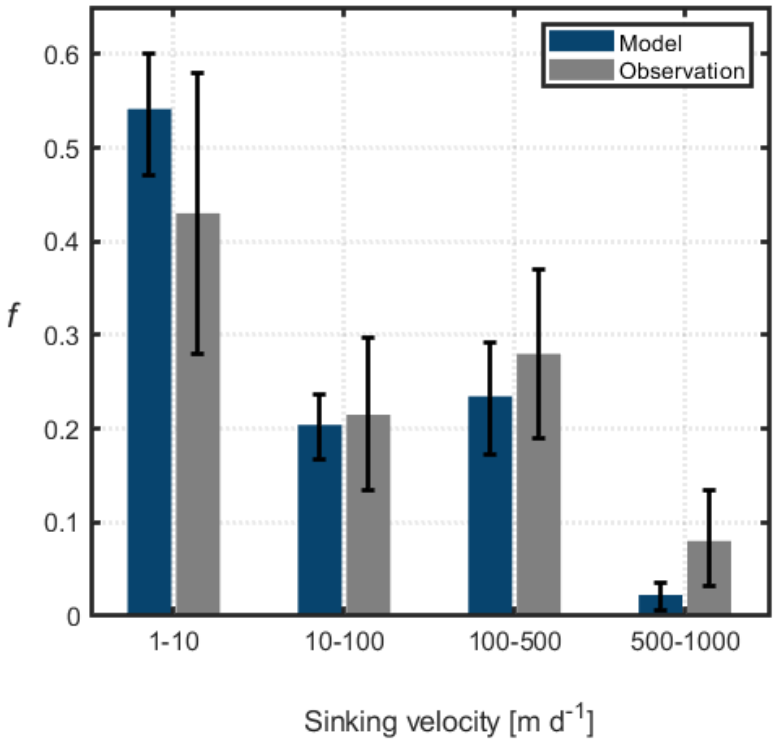

Fig. S2. Comparison of settling velocities for marine aggregates in the particle model to observed settling velocities in the modern ocean. Measured data for sinking velocity are from (*33*).

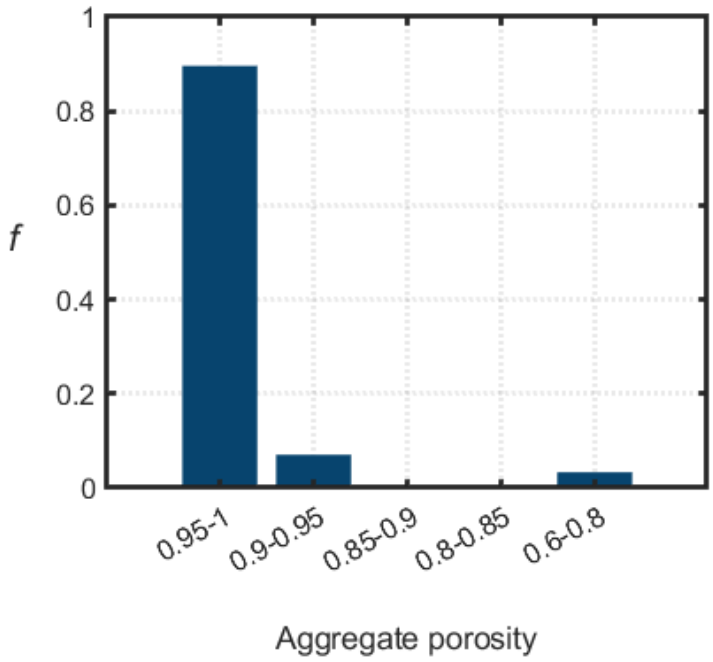

Fig. S3. Modelled porosity of the marine aggregates for the control case with no mineral addition. Model results indicate that most of the modelled marine aggregates have porosity values very close to 1.0, consistent with the observations of natural marine aggregates (*37-39*).

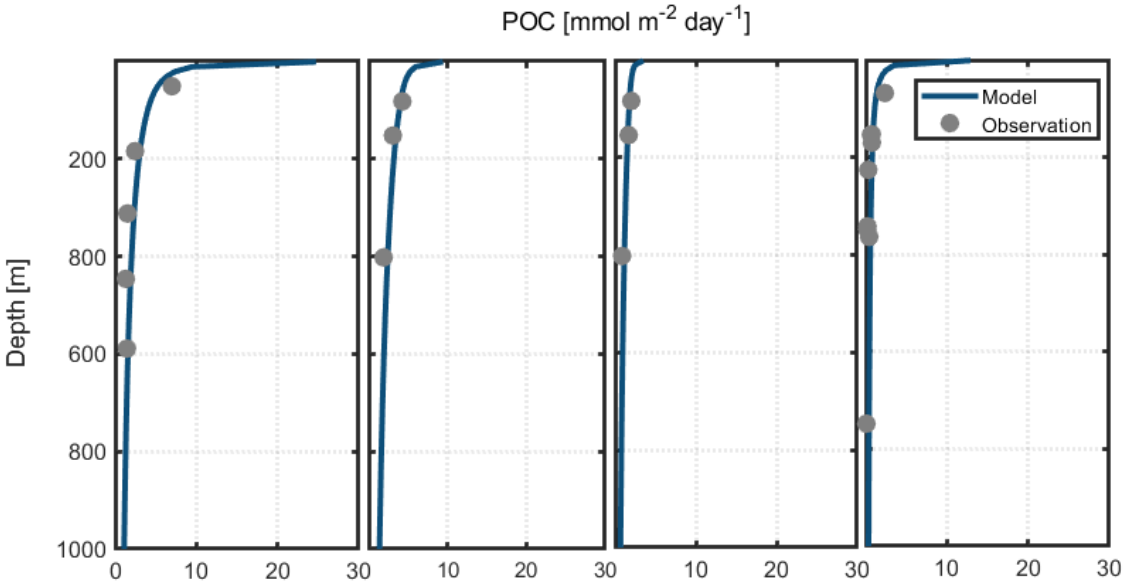

Fig. S4. Calibration results for water column abundance of particulate organic carbon (POC). Observations are derived from neutrally buoyant sediment trap data from four different sites using in the North Atlantic (*92*).

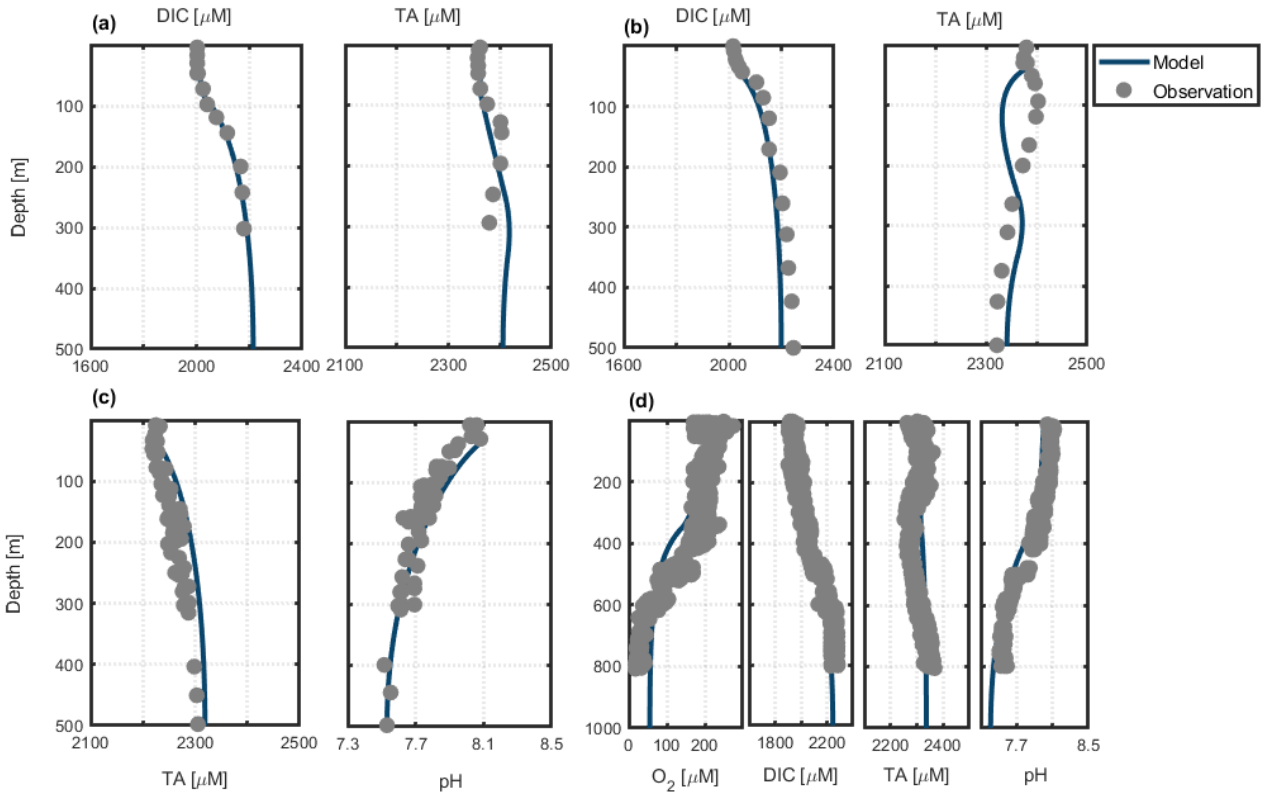

Fig. S5. Comparison of model dissolved tracers with observed water column profiles in a range of marine settings. Observations in panels (a) and (b) are from two different sites in the Gulf of Mexico (*93*), while panels (c) and (d) show observations from a costal (*94*) and an open ocean site (*32*) in pacific.

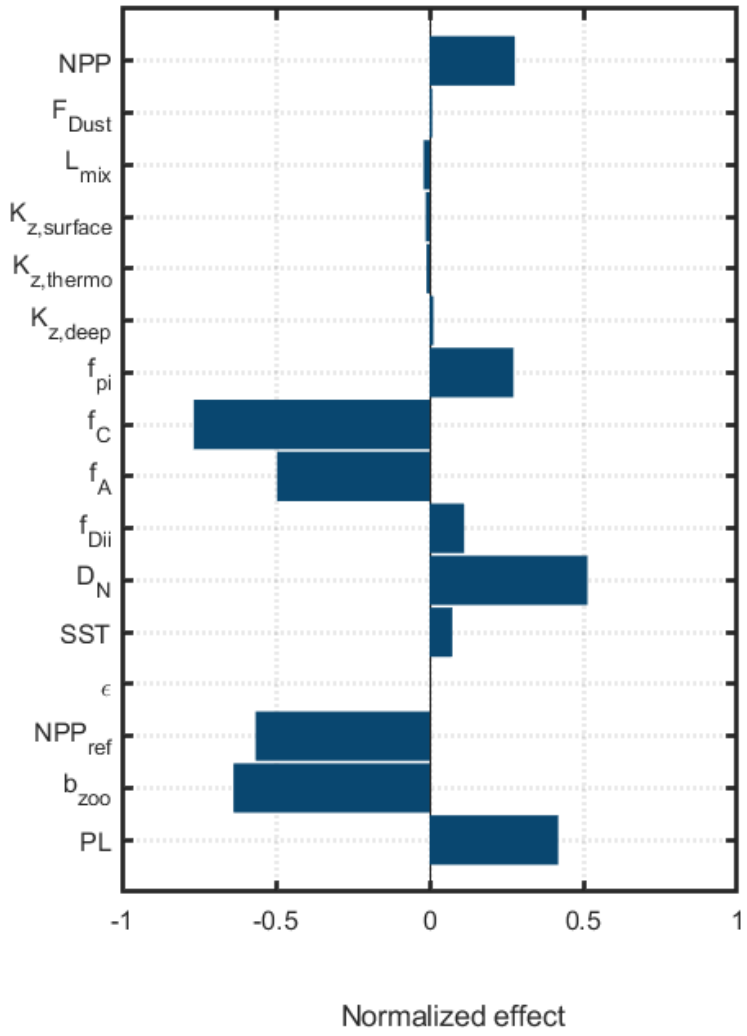

Fig. S6. Results of model sensitivity analysis showing normalized impact on average sinking rate of marine aggregates varying parameter ranges according to values shown in Table S2. While the average sinking rate of marine aggregates is largely insensitive to most model parameters, the parameters with the largest impact on the average sinking rate of marine aggregates include: the strength of marine net primary production (*NPP*) and its reference value (NPP_{ref}), fractal dimension (D_N), coefficient for the decrease of zooplankton abundance with depth (b_{zoo}), prosome length (*PL*), and fraction of NPP that is produced by picoplankton (f_{pi}), coccolithophorid (f_C), and aragonite forming phytoplankton (f_A) have the largest influence.

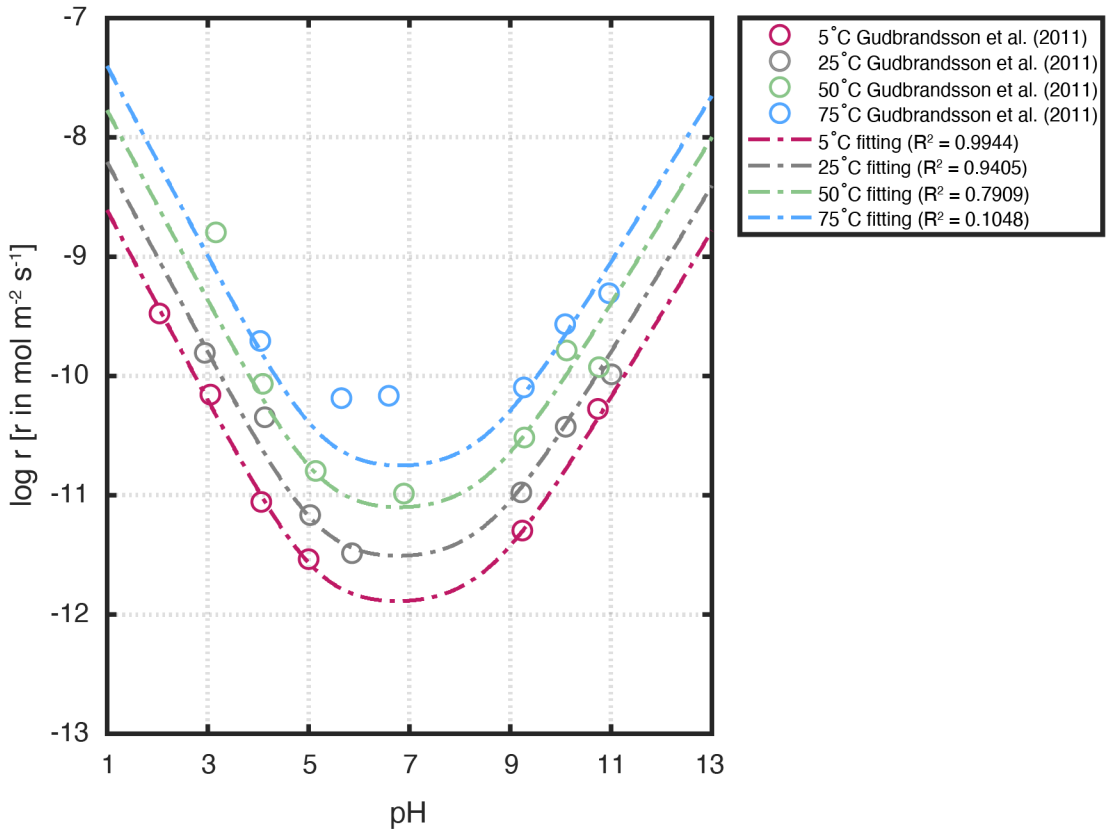

Fig. S7. Experimental rates of crystalline basalt dissolution as a function of pH and temperature. The symbols correspond to experimentally measured dissolution rates for crystalline basalt at various temperatures as a function of pH reported in the literature (*41*). The dash-dotted lines are fitted curves for crystalline basalt dissolution kinetics at various temperatures (fuchsia for 5°C, grey for 25°C, green for 50°C, and blue for 75°C) calculated using the Eq. (34) in this study. The R^2 value for each fitted regression line is labeled besides the corresponding legend. The fitted rate parameters are summarized in Table S3.

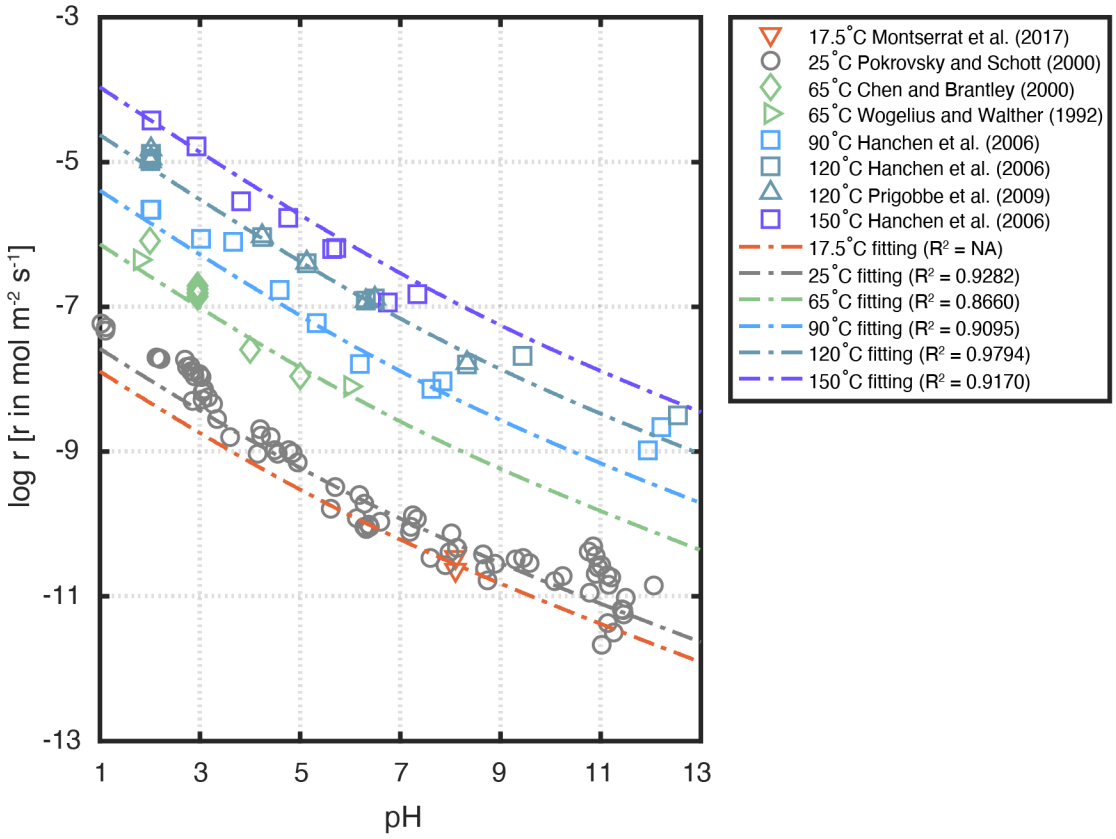

Fig. S8. Experimental rates of olivine (forsterite) dissolution as a function of pH and temperature. The symbols correspond to experimentally measured dissolution rates of forsterite (Fo) at various temperatures as a function of pH that are summarized from the literatures (*42, 43, 50, 51, 53*). The dash-dotted lines are fitted curves for forsterite dissolution kinetics at various temperatures (orange for 17.5°C, grey for 25°C, green for 65°C, blue for 90°C, indigo for 120°C, and purple for 150°C) calculated using the Eq. (36) in this study. The R^2 value (coefficient of determination) for each fitted regression line is labeled besides the corresponding legend. The fitted rate parameters are summarized in Table S3.

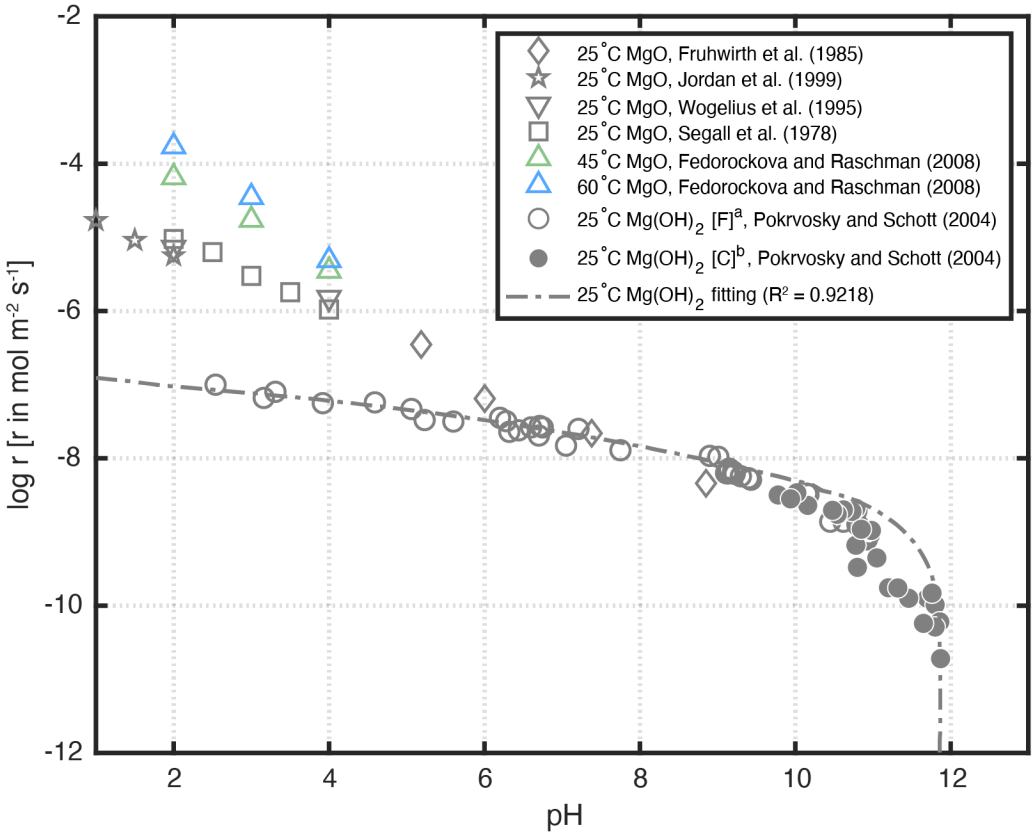

Fig. S9. Experimental rates of brucite ($Mg(OH)_2$) and periclase (MgO) dissolution as a function of pH and temperature. The circles represent experimentally measured steady-state dissolution rates of $Mg(OH)_2$ at 25°C as a function of pH from (*57*). Open circles indicate rates measured at far-from-equilibrium conditions and filled circles are measured rates at close-to-equilibrium conditions. All other symbols correspond to measured dissolution rates of MgO at various temperature and pH conditions from the literature (*54, 55, 95-97*). The dash-dotted line is the fitted curve for $Mg(OH)_2$ dissolution kinetics at 25°C calculated using Eq. (38) in this study. The fitted rate parameters are summarized in Table S3.

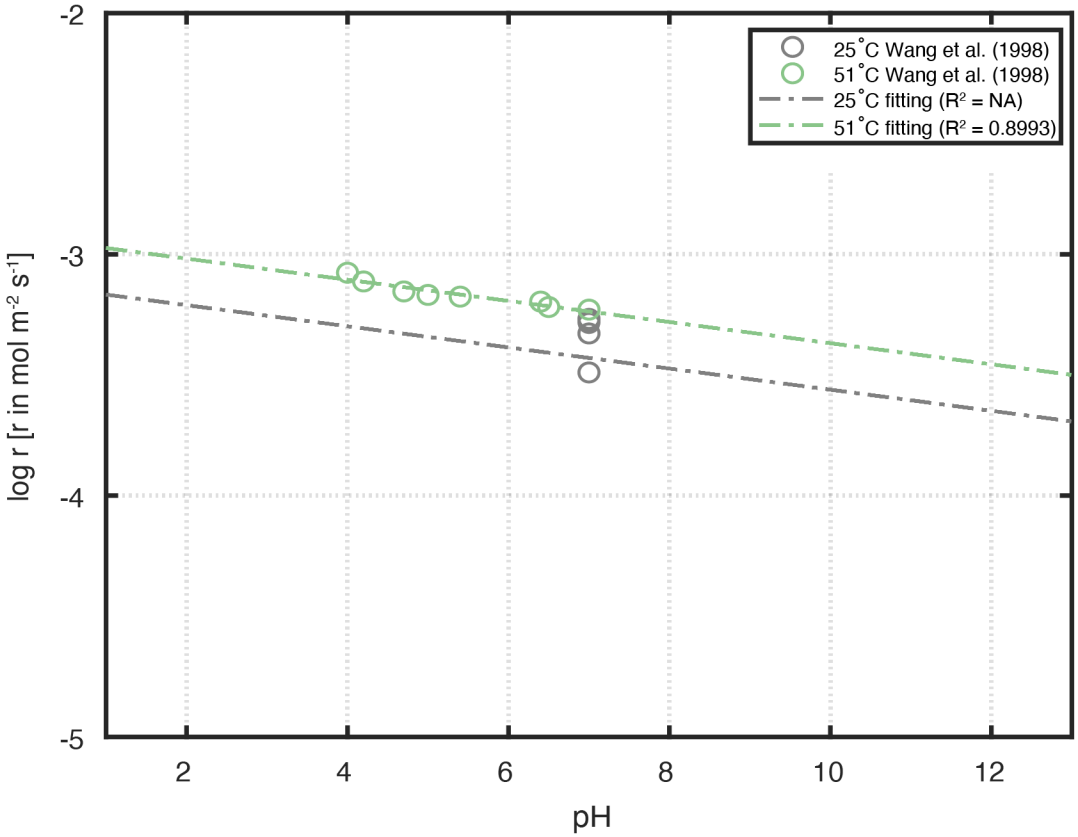

Fig. S10. Experimental rates of slaked lime ($Ca(OH)_2$) dissolution as a function of pH and temperature. The grey and green circles correspond to experimentally measured dissolution rates of $Ca(OH)_2$ at 25°C and 51°C, respectively, as a function of pH reported from the literature (*59*). The dash-dotted lines are fitted curves for $Ca(OH)_2$ dissolution kinetics at 25°C and 51°C, respectively, calculated using the Eq. (45) in this study. The fitted rate parameters are summarized in Table S3.

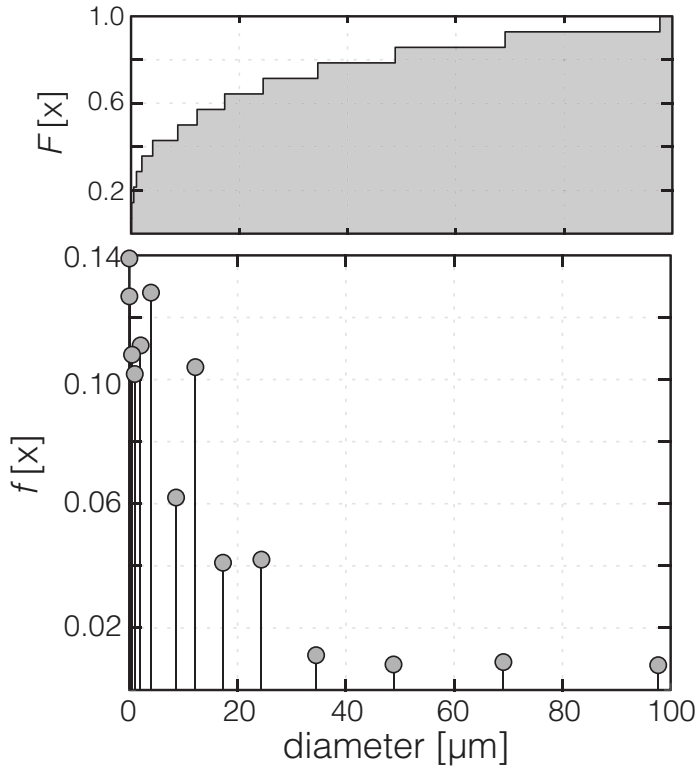

Fig. S11. Feedstock particle size distribution (PSD) used in our default model. Particle size distribution is derived from (*68*), and is shown as a discrete (binned) distribution as implemented in the model (bottom) and as a cumulative mass fraction distribution (top).

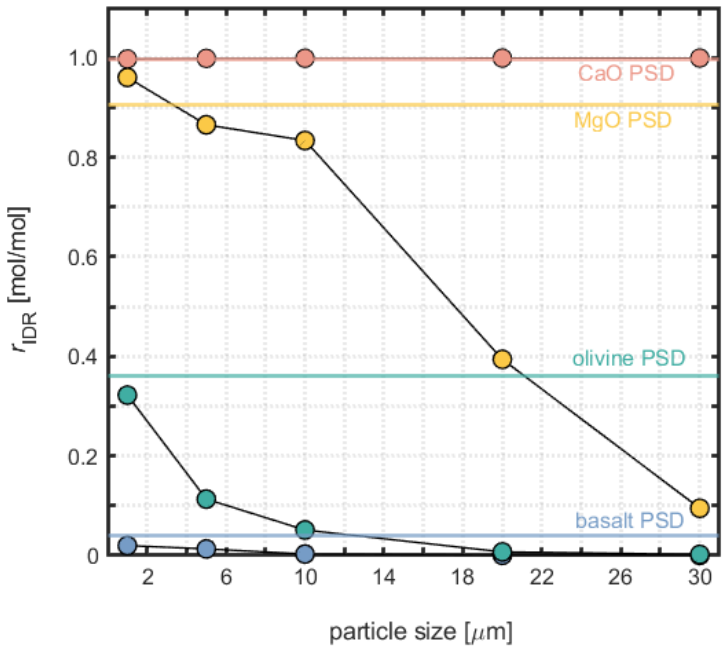

Fig. S12. The effect of mineral grain size on depth-integrated alkalinity release (r_{IDR}). Results are reported as the depth-integrated rate of mineral dissolution relative to the maximum possible depth-integrated rate of mineral dissolution where feedstock is completely dissolved in the upper water column (here between 0-80m depth). The horizontal lines (PSD) correspond to the case where a mineral size distribution instead of a fixed mineral grain size is used (see above).

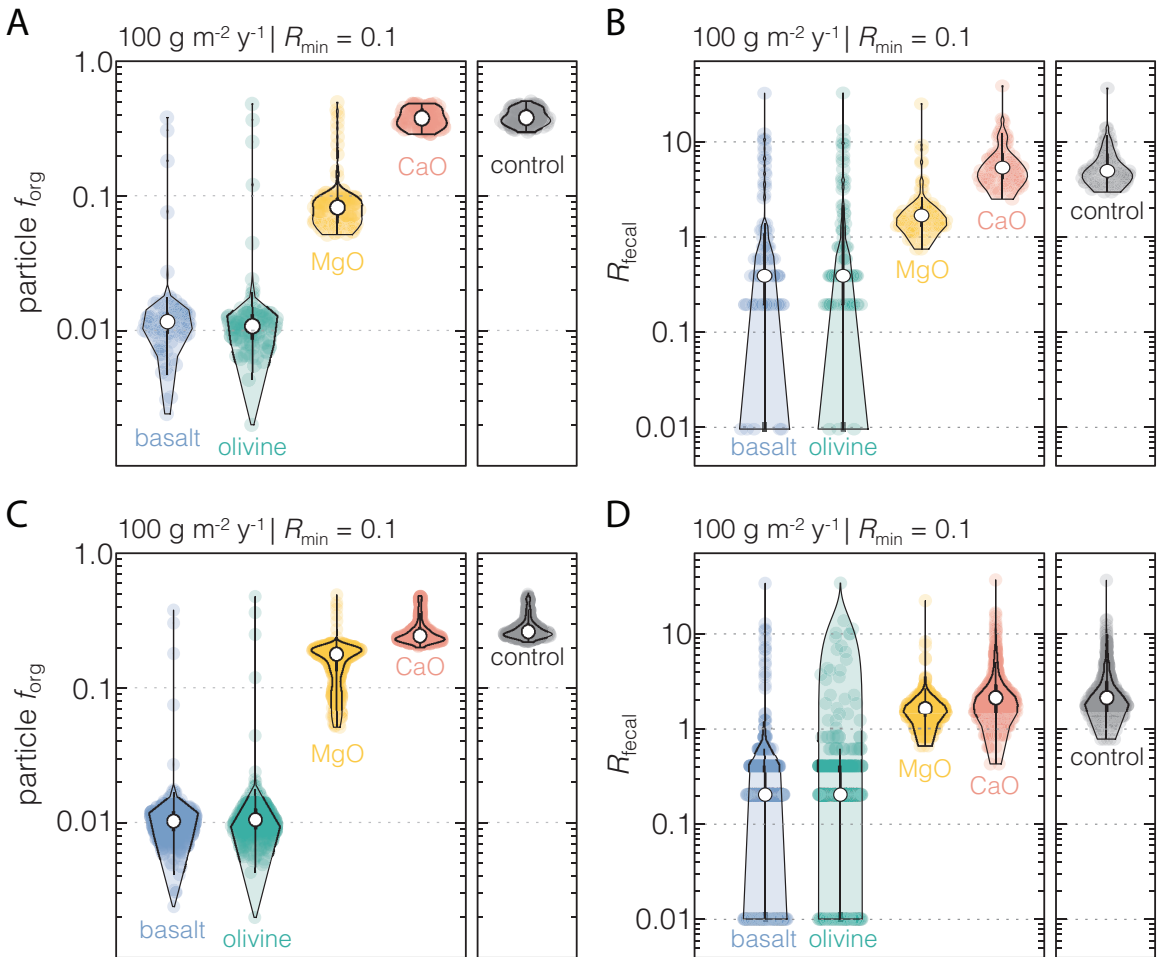

Fig. S13. Impact of operative surface ocean depth on marine particle composition and zooplankton grazing. (**A**) Values of average particle organic matter fraction (f_{org}) in the upper water column compared to those of a control simulation with no feedstock addition. Open circles show median values, while violin plots show the distribution of results across all depths within the upper 100m. Results are shown for an idealized coastal marine ecosystem with a feedstock application rate of 100 gC m^{-2} y^{-1} and a ratio between feedstock application rate and net primary productivity (R_{min}) of 0.1 (g/g). (**B**) Values of zooplankton fecal pellet production within the upper 100m of the water column compared to those of a control simulation with no feedstock addition. Fecal pellet production is given as the fraction of encounter events that lead to ingestion and fecal pellet production (R_{fecal}). (**C**) Values of average particle organic matter fraction (f_{org}) in the upper water column compared to those of a control simulation with no feedstock addition. Open circles show median values, while violin plots show the distribution of results across all depths within the upper 500m. Results are shown for an idealized coastal marine ecosystem with a feedstock application rate of 100 gC m^{-2} y^{-1} and a ratio between feedstock application rate and net primary productivity (R_{min}) of 0.1 (g/g). (**D**) Values of zooplankton fecal pellet production within the upper 500m of the water column compared to those of a control simulation with no feedstock addition. Fecal pellet production is given as the fraction of encounter events that lead to ingestion and fecal pellet production (R_{fecal}).

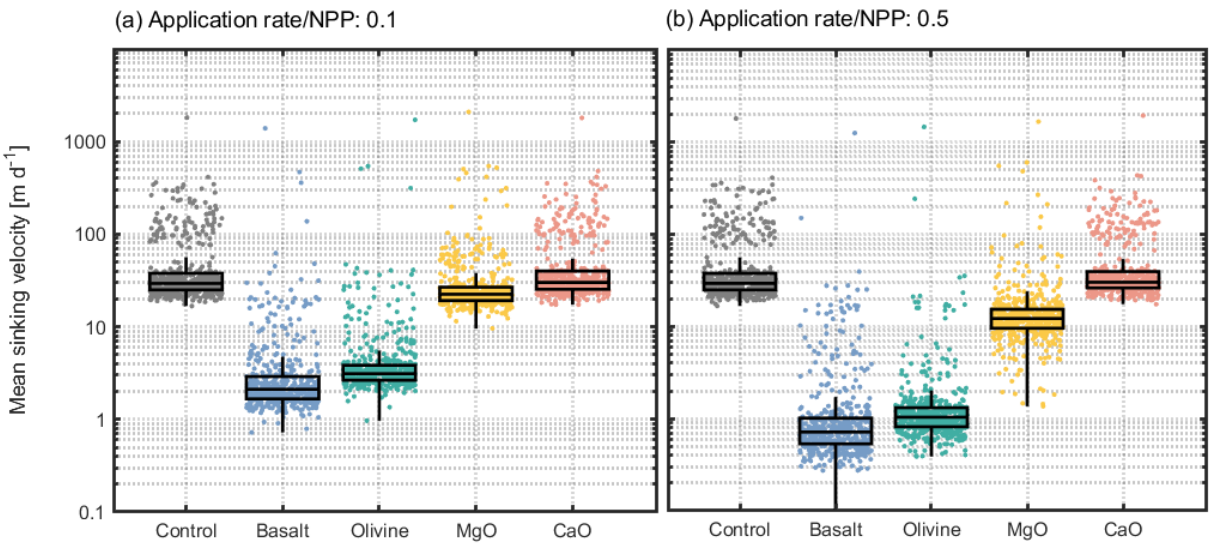

Fig. S14. The impact of mineral addition to the average sinking velocity of marine aggregates. Each point corresponds to the average sinking velocity of marine aggregates at individual depths between 0-500m. Results are shown for a ratio between feedstock application rate and net primary productivity (NPP) of 0.1 (left) and 0.5 (right).

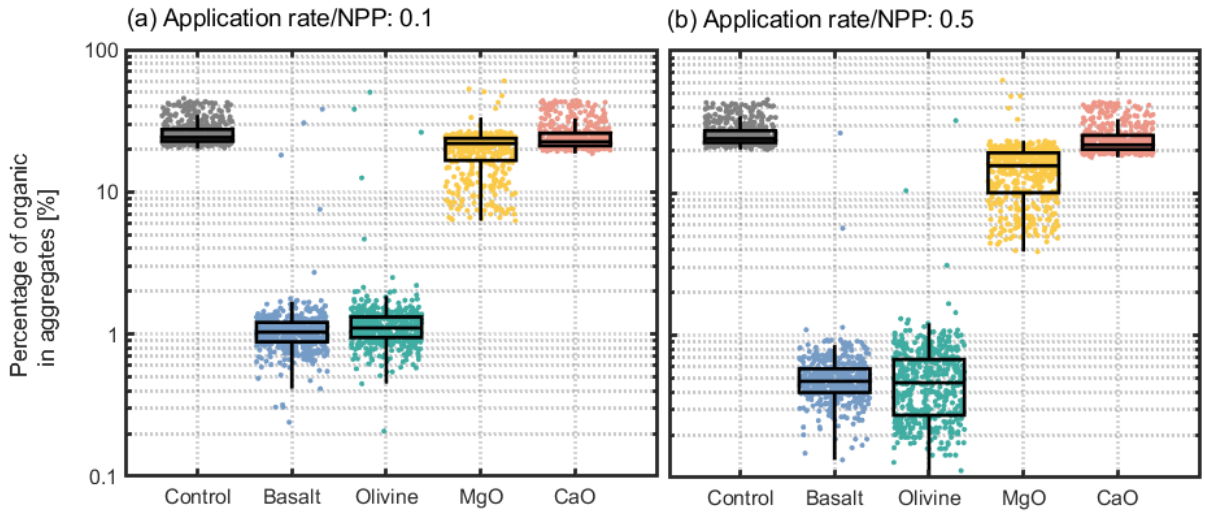

Fig. S15. The impact of mineral addition on the abundance of organic matter in marine aggregates. Each point corresponds to the average organic matter content of marine aggregates at individual depths between 0-500m. Results are shown for a ratio between feedstock application rate and net primary productivity (NPP) of 0.1 (left) and 0.5 (right).

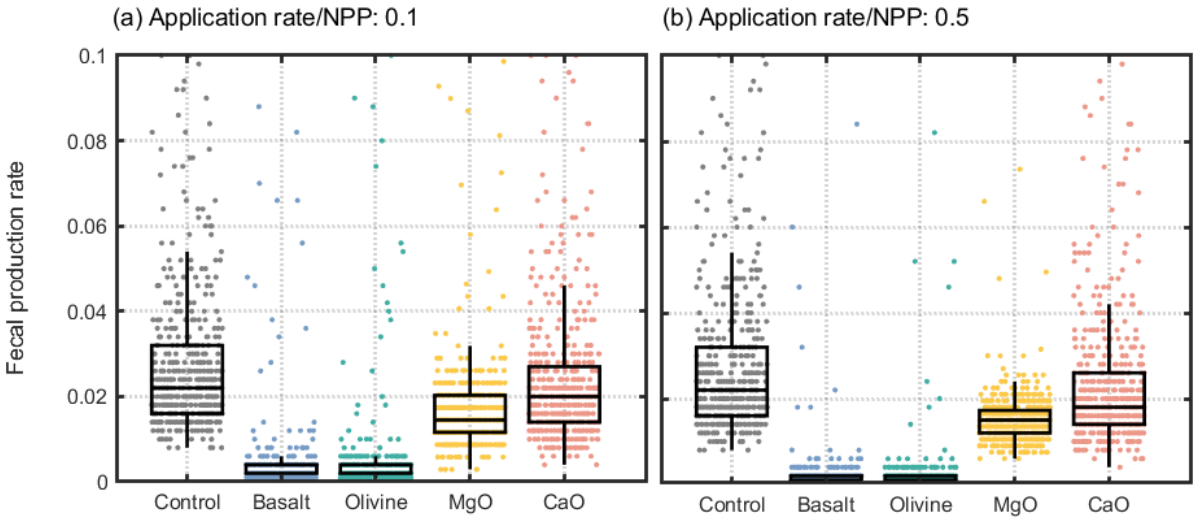

Fig. S16. The impact of mineral addition on the rate of fecal pellet production by zooplankton (a proxy for zooplankton grazing rate and overall biomass/abundance). Each point corresponds to the average zooplankton fecal pellet production rate at individual depths between 0-500m. Results are shown for a ratio between feedstock application rate and net primary productivity (NPP) of 0.1 (left) and 0.5 (right).

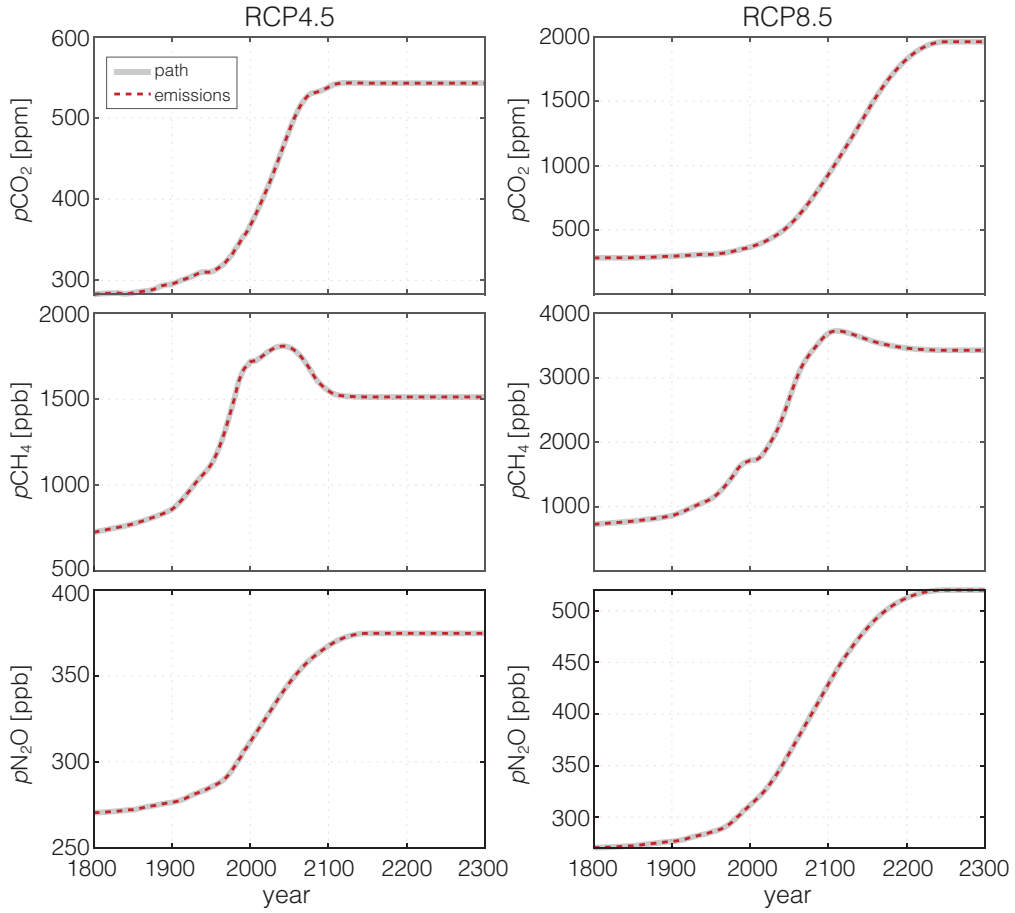

Fig. S17. Atmospheric partial pressures of carbon dioxide (pCO_2), methane (pCH_4), and nitrous oxide (pN_2O) in the control Earth system model experiments. Trajectories follow Representative Concentration Pathway (RCP) and Extended Concentration Pathway (ECP) 4.5 and 8.5 (*79*). Grey curves show simulations in which atmospheric composition is forced (restored) at each timestep according to a given pathway ('path'), while dashed red curves show simulations in which atmospheric CO_2 is driven by natural and anthropogenic emissions and atmospheric composition is calculated dynamically ('emissions'). Note that both CH_4 and N2O are concentration-driven in all simulations.

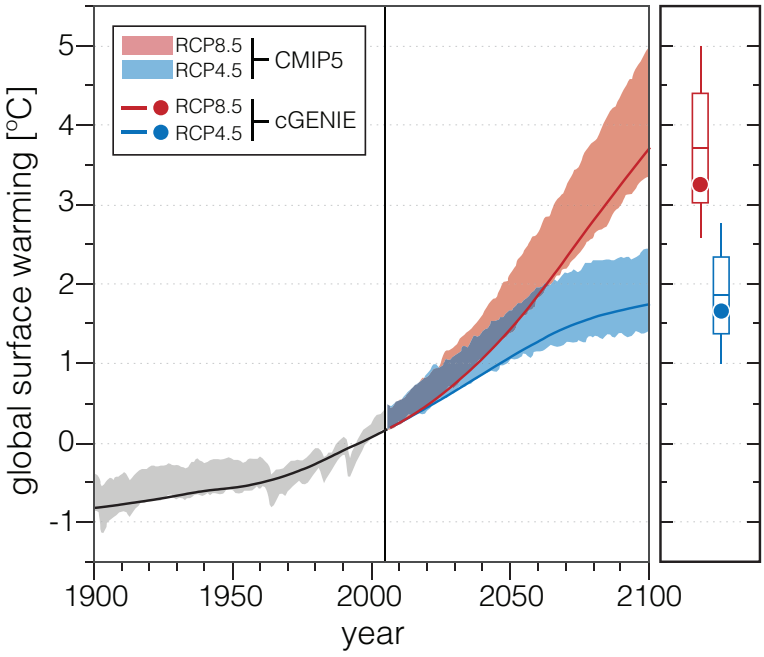

Fig. S18. Temperature trajectories for historical and future transients in the Earth system model compared to results from the Coupled Model Intercomparison Project 5 (CMIP5). Solid lines at left show cGENIE temperature trajectories for the moderate-emissions (RCP4.5) and high-emissions (RCP8.5) scenarios, while shaded regions show corresponding ranges for CMIP5 models. Box plots at right (ensemble mean, ±1SD, and minimum to maximum range) show CMIP5 results for globally averaged temperature for 2080-2099, while filled circles show cGENIE results. CMIP5 results from (*98*)

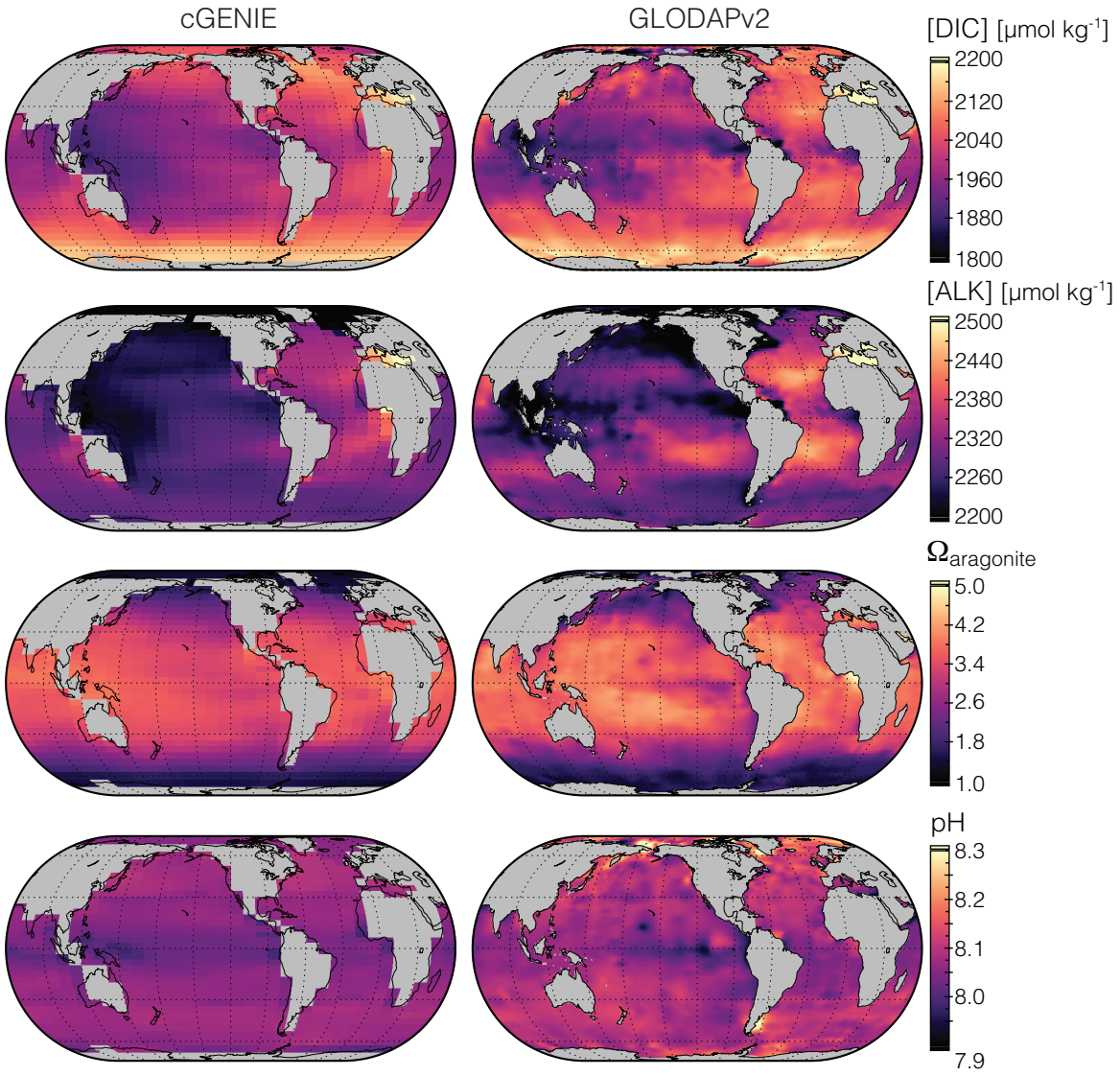

Fig. S19. Surface ocean carbonate chemistry parameters in historical cGENIE simulation compared to gridded observational data. Shown at left are year 2000 results for concentrations of dissolved inorganic carbon ([DIC]), alkalinity ([ALK]), aragonite saturation state ($\Omega_{aragonite}$), and pH. Shown on the right are observational data from the GLODAPv2 dataset (*99*).

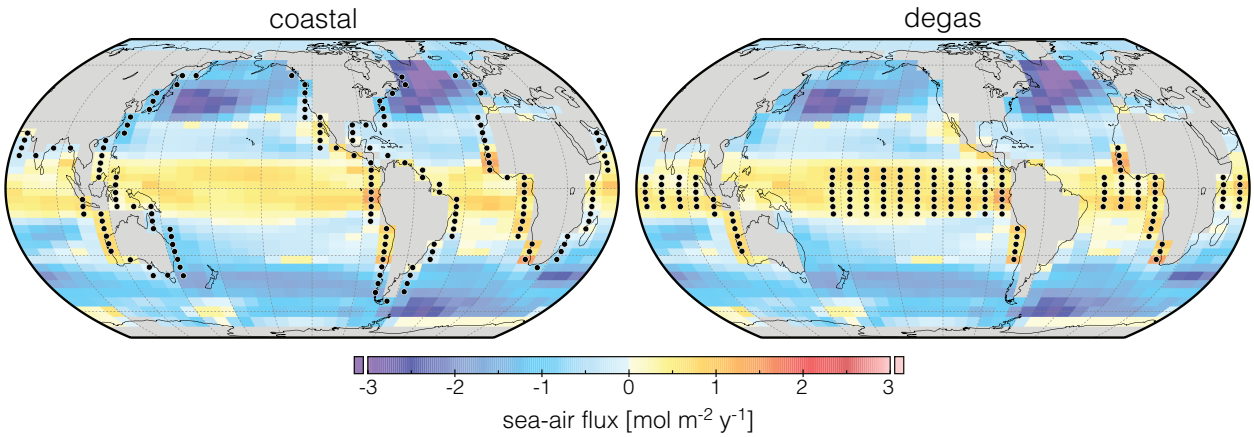

Fig. S20. Application scenarios for simulations of carbon dioxide capture (CDR) using ocean alkalinity enhancement. Filled circles show grid cells in which an alkalinity flux was applied based on results from the particle model. A global application rate was spread evenly throughout these grid cells, focused either in coastal settings ('coastal'; left) or in regions of relatively high background sea-air outgassing of CO_2 ('degas'; right). The underlying field shows the background sea-air flux of CO_2 in model year 2010.

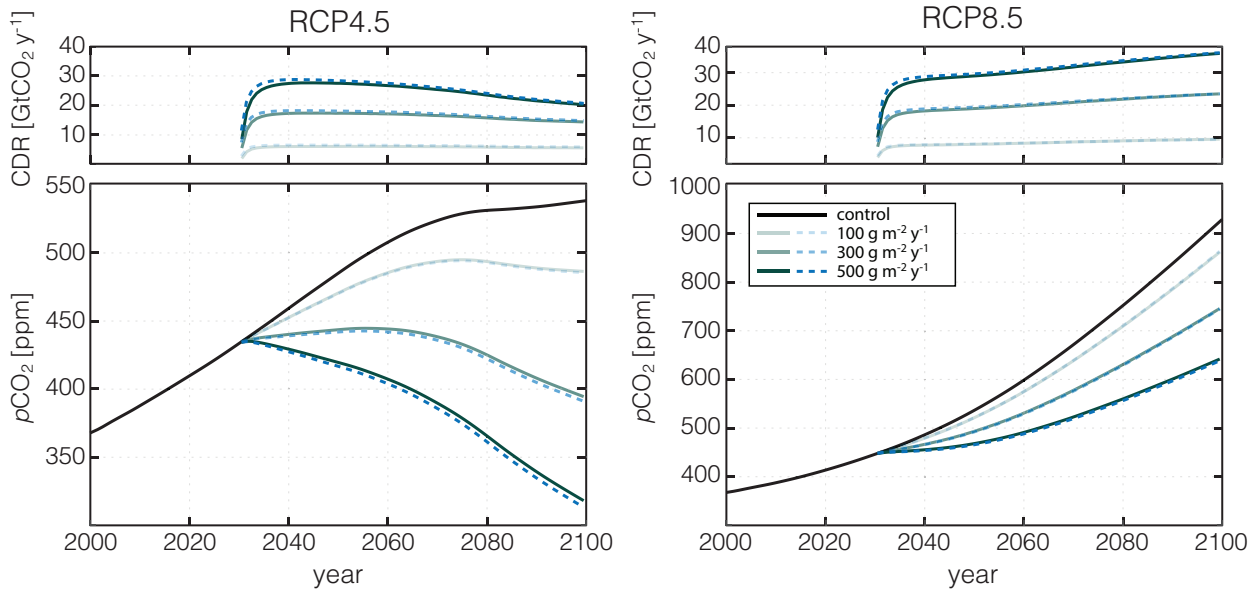

Fig. S21. Gross carbon dioxide removal (CDR) potential of ocean alkalinity enhancement using CaO as a feedstock for the 'coastal' and 'degas' scenarios. Results are shown for a moderate-emissions pathway (RCP4.5; left) and a high-emissions pathway (RCP8.5; right). Top panels show rates of CDR over time, computed as the difference in air-sea CO_2 flux relative to a control simulation with no alkalinity addition. Bottom panels show partial pressure of atmospheric CO_2 (pCO_2) over time for the same feedstock amendment rates (green, blue), compared to a control simulation with no alkalinity addition (black). Results are shown for "low" (100 g m^{-2} y^{-1}), "moderate" (300 g m^{-2} y^{-1}), and "high" (500 g m^{-2} y^{-1}) rates of CaO addition. Dashed blue lines show results for "coastal" scenario, while solid green lines show results for "degas" scenario.

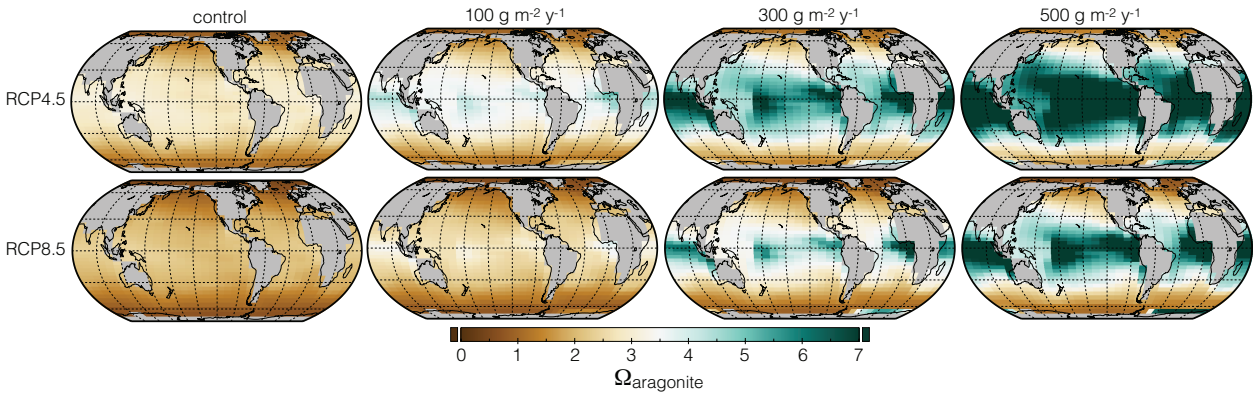

Fig. S22. End-of-century (2100) surface ocean aragonite saturation state during ocean alkalinity enhancement using CaO as a feedstock for the 'degas' scenario. Results are shown for a moderate-emissions pathway (RCP4.5; top) and a high-emissions pathway (RCP8.5; bottom), with increasing CaO application rate increasing from left to right.

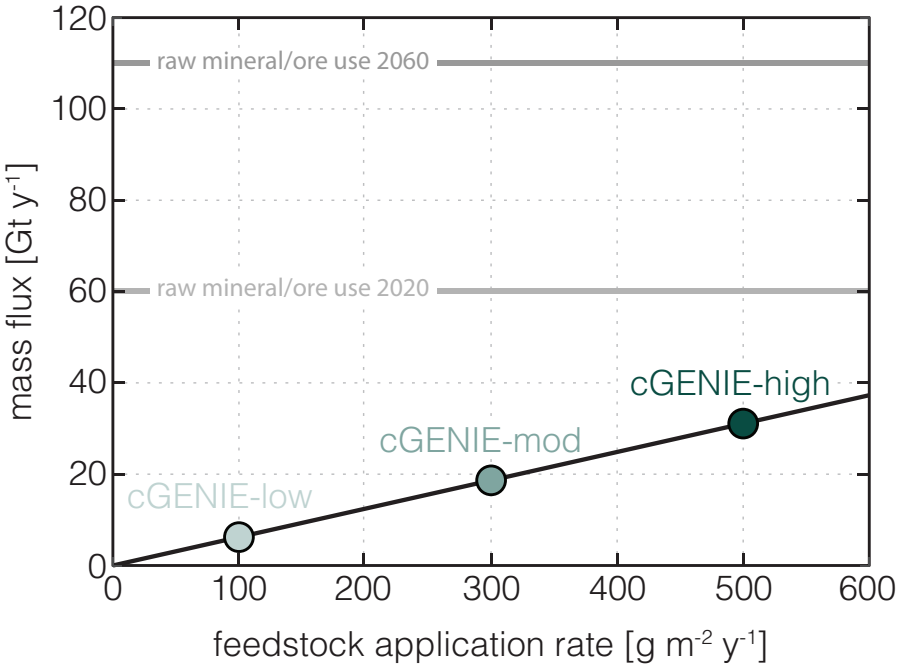

Fig. S23. Feedstock application rates used for simulations of carbon dioxide capture (CDR) using CaO as a feedstock for ocean alkalinity enhancement. Black curve shows the globally integrated feedstock mass flux (in Gt of feedstock per year implied by a given feedstock application rate (area-normalized) when scaled to the application areas shown in Fig. S17. Filled circles show fluxes for the "low", "moderate", and "high" application scenarios discussed in the Main Text. Also shown are estimates of raw mineral (non-metallic) and ore use in 2020 (*81*) and as projected for 2060 (*82*).

References:

1. M. Fakhraee, N. J. Planavsky, C. T. Reinhard, The role of environmental factors in the long-term evolution of the marine biological pump. *Nature Geoscience* **13**, 812-816 (2020).
2. M. Fakhraee, L. G. Tarhan, N. J. Planavsky, C. T. Reinhard, A largely invariant marine dissolved organic carbon reservoir across Earth's history. *Proceedings of the National Academy of Sciences* **118**, e2103511118 (2021).
3. T. Jokulsdottir, D. Archer, A stochastic, Lagrangian model of sinking biogenic aggregates in the ocean (SLAMS 1.0): model formulation, validation and sensitivity. *Geoscientific Model Development* **9**, 1455-1476 (2016).
4. J. H. Martin, G. A. Knauer, W. W. Broenkow, VERTEX: the lateral transport of manganese in the northeast Pacific. *Deep Sea Research Part A. Oceanographic Research Papers* **32**, 1405-1427 (1985).
5. T. Jokulsdottir, D. Archer, A stochastic, Lagrangian model of sinking biogenic aggregates in the ocean (SLAMS 1.0): model formulation, validation and sensitivity. *Geosci. Model Dev.* **9**, 1455-1476 (2016).
6. A. Burd, G. A. Jackson, Predicting particle coagulation and sedimentation rates for a pulsed input. *Journal of Geophysical Research: Oceans* **102**, 10545-10561 (1997).
7. A. B. Burd, G. A. Jackson, Particle Aggregation. *Annual Review of Marine Science* **1**, 65-90 (2009).
8. X. Li, B. E. Logan, Size distributions and fractal properties of particles during a simulated phytoplankton bloom in a mesocosm. *Deep Sea Research Part II: Topical Studies in Oceanography* **42**, 125-138 (1995).
9. B. E. Logan, D. B. Wilkinson, Fractal geometry of marine snow and other biological aggregates. *Limnology and Oceanography* **35**, 130-136 (1990).
10. T. W. Trull *et al.*, In situ measurement of mesopelagic particle sinking rates and the control of carbon transfer to the ocean interior during the Vertical Flux in the Global Ocean (VERTIGO) voyages in the North Pacific. *Deep Sea Research Part II: Topical Studies in Oceanography* **55**, 1684-1695 (2008).
11. W. M. Berelson, Particle settling rates increase with depth in the ocean. *Deep Sea Research Part II: Topical Studies in Oceanography* **49**, 237-251 (2001).
12. A. L. Alldredge, T. C. Granata, C. C. Gotschalk, T. D. Dickey, The physical strength of marine snow and its implications for particle disaggregation in the ocean. *Limnology and Oceanography* **35**, 1415-1428 (1990).
13. F. M. White, *Fluid Mechanics, 5th Edition*. McGraw-Hill Series in Mechanical Engineering (McGraw-Hill, 2002).
14. N. E. Dorsey, *Properties of ordinary water-substance in all its phases: water-vapour, water and all the ices*. American Chemical Society Monograph Series No. 81 (New York: Reinhold Publishing Corporation, 1940).
15. J. T. Turner, Zooplankton fecal pellets, marine snow, phytodetritus and the ocean's biological pump. *Progress in Oceanography* **130**, 205-248 (2015).
16. D. K. Steinberg, M. R. Landry, Zooplankton and the Ocean Carbon Cycle. *Annual Review of Marine Science* **9**, 413-444 (2017).
17. N. Briggs, G. Dall'Olmo, H. Claustre, Major role of particle fragmentation in regulating biological sequestration of CO2 by the oceans. *Science* **367**, 791-793 (2020).
18. M. H. Iversen *et al.*, Sinkers or floaters? Contribution from salp pellets to the export flux during a large bloom event in the Southern Ocean. *Deep Sea Research Part II: Topical Studies in Oceanography* **138**, 116-125 (2017).
19. S. Hernández-León *et al.*, Large deep-sea zooplankton biomass mirrors primary production in the global ocean. *Nature Communications* **11**, 6048 (2020).
20. A. Forest *et al.*, Size distribution of particles and zooplankton across the shelf-basin system in southeast Beaufort Sea: combined results from an Underwater Vision Profiler and vertical net tows.

Biogeosciences **9**, 1301-1320 (2012).
21. S. Goldthwait, J. Yen, J. Brown, A. Alldredge, Quantification of marine snow fragmentation by swimming euphausiids. *Limnology and Oceanography* **49**, 940-952 (2004).
22. H. Ploug, M. H. Iversen, G. Fischer, Ballast, sinking velocity, and apparent diffusivity within marine snow and zooplankton fecal pellets: Implications for substrate turnover by attached bacteria. *Limnology and Oceanography* **53**, 1878-1886 (2008).
23. S.-i. Uye, K. Kaname, Relations between fecal pellet volume and body size for major zooplankters of the Inland Sea of Japan. *Journal of Oceanography* **50**, 43-49 (1994).
24. J. J. Middelburg, A simple rate model for organic matter decomposition in marine sediments. *Geochimica et Cosmochimica Acta* **53**, 1577-1581 (1989).
25. S. Katsev, S. A. Crowe, Organic carbon burial efficiencies in sediments: The power law of mineralization revisited. *Geology* **43**, 607-610 (2015).
26. J. I. Hedges, R. G. Keil, Sedimentary organic matter preservation: an assessment and speculative synthesis. *Marine Chemistry* **49**, 81-115 (1995).
27. G. Hulthe, S. Hulth, P. O. J. Hall, Effect of oxygen on degradation rate of refractory and labile organic matter in continental margin sediments. *Geochimica et Cosmochimica Acta* **62**, 1319-1328 (1998).
28. D. J. Burdige, Preservation of Organic Matter in Marine Sediments: Controls, Mechanisms, and an Imbalance in Sediment Organic Carbon Budgets? *Chemical Reviews* **107**, 467-485 (2007).
29. J. A. Cram *et al.*, The Role of Particle Size, Ballast, Temperature, and Oxygen in the Sinking Flux to the Deep Sea. *Global Biogeochemical Cycles* **32**, 858-876 (2018).
30. A. V. Quinlan, The thermal sensitivity of generic Michaelis-Menten processes without catalyst denaturation or inhibition. *Journal of Thermal Biology* **6**, 103-114 (1981).
31. A. V. Quinlan, The Thermal Sensitivity of Michaelis-Menten Kinetics as a Function of Substrate Concentration. *Journal of the Franklin Institute* **310**, 325-342 (1980).
32. J. E. Dore, R. Lukas, D. W. Sadler, M. J. Church, D. M. Karl, Physical and biogeochemical modulation of ocean acidification in the central North Pacific. *Proceedings of the National Academy of Sciences* **106**, 12235-12240 (2009).
33. I. J. Alonso-González *et al.*, Role of slowly settling particles in the ocean carbon cycle. *Geophys Res Lett* **37**, (2010).
34. G. Fischer, G. Karakaş, Sinking rates and ballast composition of particles in the Atlantic Ocean: implications for the organic carbon fluxes to the deep ocean. *Biogeosciences* **6**, 85-102 (2009).
35. A. M. P. McDonnell, K. O. Buesseler, Variability in the average sinking velocity of marine particles. *Limnology and Oceanography* **55**, 2085-2096 (2010).
36. E. C. Laurenceau-Cornec, T. W. Trull, D. M. Davies, C. L. De La Rocha, S. Blain, Phytoplankton morphology controls on marine snow sinking velocity. *Marine Ecology Progress Series* **520**, 35-56 (2015).
37. M. Kajihara, Settling velocity and porosity of large suspended particle. *Journal of the Oceanographical Society of Japan* **27**, 158-162 (1971).
38. A. L. Alldredge, C. Gotschalk, In situ settling behavior of marine snow1. *Limnology and Oceanography* **33**, 339-351 (1988).
39. S. MacIntyre, A. L. Alldredge, C. C. Gotschalk, Accumulation of marines now at density discontinuities in the water column. *Limnology and Oceanography* **40**, 449-468 (1995).
40. J. L. Palandri, Y. K. Kharaka, "A compilation of rate parameters of water-mineral interaction kinetics for application to geochemical modeling," *Open-File Report* (2004).
41. S. Gudbrandsson, D. Wolff-Boenisch, S. R. Gislason, E. H. Oelkers, An experimental study of crystalline basalt dissolution from 2⩽pH⩽11 and temperatures from 5 to 75°C. *Geochimica et Cosmochimica Acta* **75**, 5496-5509 (2011).
42. R. A. Wogelius, J. V. Walther, Olivine dissolution at 25°C: Effects of pH, CO2, and organic acids. *Geochimica et Cosmochimica Acta* **55**, 943-954 (1991).

43. O. S. Pokrovsky, J. Schott, Kinetics and mechanism of forsterite dissolution at 25°C and pH from 1 to 12. *Geochimica et Cosmochimica Acta* **64**, 3313-3325 (2000).
44. S. V. Golubev, O. S. Pokrovsky, J. Schott, Experimental determination of the effect of dissolved CO2 on the dissolution kinetics of Mg and Ca silicates at 25 °C. *Chemical Geology* **217**, 227-238 (2005).
45. L. Marini, *Geological sequestration of carbon dioxide: thermodynamics, kinetics, and reaction path modeling*. (Elsevier, 2006).
46. S. L. Brantley, J. D. Kubicki, A. F. White, *Kinetics of water-rock interaction*. (Springer, 2008), vol. 168.
47. J. D. Rimstidt, S. L. Brantley, A. A. Olsen, Systematic review of forsterite dissolution rate data. *Geochimica et Cosmochimica Acta* **99**, 159-178 (2012).
48. F. K. Crundwell, The mechanism of dissolution of forsterite, olivine and minerals of the orthosilicate group. *Hydrometallurgy* **150**, 68-82 (2014).
49. E. H. Oelkers, J. Declercq, G. D. Saldi, S. R. Gislason, J. Schott, Olivine dissolution rates: A critical review. *Chemical Geology* **500**, 1-19 (2018).
50. M. Hänchen, V. Prigiobbe, G. Storti, T. M. Seward, M. Mazzotti, Dissolution kinetics of fosteritic olivine at 90–150°C including effects of the presence of CO2. *Geochimica et Cosmochimica Acta* **70**, 4403-4416 (2006).
51. V. Prigiobbe, G. Costa, R. Baciocchi, M. Hänchen, M. Mazzotti, The effect of CO2 and salinity on olivine dissolution kinetics at 120∘C. *Chemical Engineering Science* **64**, 3510-3515 (2009).
52. F. Montserrat *et al.*, Olivine Dissolution in Seawater: Implications for CO2 Sequestration through Enhanced Weathering in Coastal Environments. *Environ Sci Technol* **51**, 3960-3972 (2017).
53. Y. Chen, S. L. Brantley, Dissolution of forsteritic olivine at 65°C and 2<pH<5. *Chemical Geology* **165**, 267-281 (2000).
54. O. Fruhwirth, G. W. Herzog, I. Hollerer, A. Rachetti, Dissolution and hydration kinetics of MgO. *Surface Technology* **24**, 301-317 (1985).
55. R. A. Wogelius, K. Refson, D. G. Fraser, G. W. Grime, J. P. Goff, Periclase surface hydroxylation during dissolution. *Geochimica et Cosmochimica Acta* **59**, 1875-1881 (1995).
56. N. McQueen, P. Kelemen, G. Dipple, P. Renforth, J. Wilcox, Ambient weathering of magnesium oxide for CO2 removal from air. *Nature Communications* **11**, 3299 (2020).
57. O. S. Pokrovsky, J. Schott, Experimental study of brucite dissolution and precipitation in aqueous solutions: surface speciation and chemical affinity control. *Geochimica et Cosmochimica Acta* **68**, 31-45 (2004).
58. T. C. Keener, S. J. Khang, J. Wang. (1995).
59. J. U. N. Wang, T. C. Keener, G. Li, S.-J. Khang, The dissolution rate of Ca(OH)2 in aqueous solutions. *Chemical Engineering Communications* **169**, 167-184 (1998).
60. S. M. Mgabhi, (2021).
61. B. A. Xu, D. E. Giles, I. M. Ritchie, Reactions of lime with carbonate-containing solutions. *Hydrometallurgy* **48**, 205-224 (1998).
62. C. E. Boyd, C. S. Tucker, B. Somridhivej, Alkalinity and Hardness: Critical but Elusive Concepts in Aquaculture. *Journal of the World Aquaculture Society* **47**, 6-41 (2016).
63. L. Bernard, M. Freche, J. L. Lacout, B. Biscans, Modeling of the dissolution of calcium hydroxyde in the preparation of hydroxyapatite by neutralization. *Chemical Engineering Science* **55**, 5683-5692 (2000).
64. P. Köhler, J. F. Abrams, C. Völker, J. Hauck, D. A. Wolf-Gladrow, Geoengineering impact of open ocean dissolution of olivine on atmospheric CO 2 , surface ocean pH and marine biology. *Environmental Research Letters* **8**, 014009 (2013).
65. O. D. Neikov, D. V. Lotsko, V. G. Gopienko, in *Handbook of Non-Ferrous Metal Powders,* O. D. Neikov *et al.*, Eds. (Elsevier, Oxford, 2009), pp. 7-44.
66. O. D. Neikov, in *Handbook of Non-Ferrous Metal Powders,* O. D. Neikov *et al.*, Eds. (Elsevier,

Oxford, 2009), pp. 47-62.
67. D. J. Beerling *et al.*, Potential for large-scale CO2 removal via enhanced rock weathering with croplands. *Nature* **583**, 242-248 (2020).
68. P. Renforth, The potential of enhanced weathering in the UK. *International Journal of Greenhouse Gas Control* **10**, 229-243 (2012).
69. A. L. Lewis *et al.*, Effects of mineralogy, chemistry and physical properties of basalts on carbon capture potential and plant-nutrient element release via enhanced weathering. *Applied Geochemistry* **132**, 105023 (2021).
70. R. Cepuritis, E. J. Garboczi, C. F. Ferraris, S. Jacobsen, B. E. Sørensen, Measurement of particle size distribution and specific surface area for crushed concrete aggregate fines. *Advanced Powder Technology* **28**, 706-720 (2017).
71. H. Sun *et al.*, Jet mill grinding of portland cement, limestone, and fly ash: Impact on particle size, hydration rate, and strength. *Cement and Concrete Composites* **44**, 41-49 (2013).
72. L. Cao *et al.*, The role of ocean transport in the uptake of anthropogenic CO2. *Biogeosciences* **6**, 375-390 (2009).
73. A. Ridgwell *et al.*, Marine geochemical data assimilation in an efficient Earth System Model of global biogeochemical cycling. *Biogeosciences* **4**, 87-104 (2007).
74. N. R. Edwards, R. Marsh, Uncertainties due to transport-parameter sensitivity in an efficient 3-D ocean-climate model. *Climate Dynamics* **24**, 415-433 (2005).
75. R. Marsh, S. A. Müller, A. Yool, N. R. Edwards, Incorporation of the C-GOLDSTEIN efficient climate model into the GENIE framework: "eb_go_gs" configurations of GENIE. *Geosci. Model Dev.* **4**, 957-992 (2011).
76. S. M. Griffies, The Gent–McWilliams Skew Flux. *Journal of Physical Oceanography* **28**, 831-841 (1998).
77. A. Ridgwell, I. Zondervan, J. C. Hargreaves, J. Bijma, T. M. Lenton, Assessing the potential long-term increase of oceanic fossil fuel CO₂ uptake due to CO₂-calcification feedback. *Biogeosciences* **4**, 481-492 (2007).
78. C. T. Reinhard *et al.*, Oceanic and atmospheric methane cycling in the cGENIE Earth system model – release v0.9.14. *Geosci. Model Dev.* **13**, 5687-5706 (2020).
79. M. Meinshausen *et al.*, The RCP greenhouse gas concentrations and their extensions from 1765 to 2300. *Climatic Change* **109**, 213 (2011).
80. C. de Boyer Montégut, G. Madec, A. S. Fischer, A. Lazar, D. Iudicone, Mixed layer depth over the global ocean: An examination of profile data and a profile-based climatology. *Journal of Geophysical Research: Oceans* **109**, (2004).
81. C. Economy, "The Circularity Gap Report 2020," (2020).
82. OECD, *"Global Material Resources Outlook to 2060: Economic Drivers and Environmental Consequences"*. (Paris, 2019).
83. M. C. Summaries, Mineral Commodity Summaries; USGS Unnumbered Series. *US Geological Survey: Reston, VA*, 200 (2021).
84. P. Renforth, The negative emission potential of alkaline materials. *Nature Communications* **10**, 1401 (2019).
85. Z. Cao *et al.*, The sponge effect and carbon emission mitigation potentials of the global cement cycle. *Nature Communications* **11**, 3777 (2020).
86. N. Storni, S. Caserini, M. Grosso, The availability of limestone and other raw materials for ocean alkalinity enhancement. *Global Biogeochemical Cycles*, (In revision).
87. Z. V. Finkel, in *Global Environmental Change,* B. Freedman, Ed. (Springer Netherlands, Dordrecht, 2014), pp. 117-124.
88. T. L. Péwé, *Desert Dust: Origin, Characteristics, and Effect on Man*. (Geological Society of America, 1981).
89. K. Ozaki, E. Tajika, Biogeochemical effects of atmospheric oxygen concentration, phosphorus

weathering, and sea-level stand on oceanic redox chemistry: Implications for greenhouse climates. *Earth and Planetary Science Letters* **373**, 129-139 (2013).
90. S. Katsev, D. G. Rancourt, I. L'Heureux, dSED: a database tool for modeling sediment early diagenesis. *Computers & Geosciences* **30**, 959-967 (2004).
91. D. E. Giles, I. M. Ritchie, B. A. Xu, The kinetics of dissolution of slaked lime. *Hydrometallurgy* **32**, 119-128 (1993).
92. C. M. Marsay *et al.*, Attenuation of sinking particulate organic carbon flux through the mesopelagic ocean. *Proceedings of the National Academy of Sciences* **112**, 1089-1094 (2015).
93. F. A. Gomez, R. Wanninkhof, L. Barbero, S. K. Lee, F. J. Hernandez Jr, Seasonal patterns of surface inorganic carbon system variables in the Gulf of Mexico inferred from a regional high-resolution ocean biogeochemical model. *Biogeosciences* **17**, 1685-1700 (2020).
94. C. E. Gómez, L. Wickes, D. Deegan, P. J. Etnoyer, E. E. Cordes, Growth and feeding of deep-sea coral Lophelia pertusa from the California margin under simulated ocean acidification conditions. *PeerJ* **6**, e5671-e5671 (2018).
95. R. L. Segall, R. S. C. Smart, P. S. Turner, Ionic oxides: distinction between mechanisms and surface roughening effects in the dissolution of magnesium oxide. *Journal of the Chemical Society, Faraday Transactions 1: Physical Chemistry in Condensed Phases* **74**, 2907-2912 (1978).
96. G. Jordan, S. R. Higgins, C. M. Eggleston, Dissolution of the periclase (001) surface; a scanning force microscope study. *American Mineralogist* **84**, 144-151 (1999).
97. A. Fedoročková, P. Raschman, Effects of pH and acid anions on the dissolution kinetics of MgO. *Chemical Engineering Journal* **143**, 265-272 (2008).
98. R. Knutti, J. Sedlácek, Robustness and uncertainties in the new CMIP5 climate model projections. *Nature Climate Change* **3**, 369-373 (2012).
99. A. Olsen *et al.*, The Global Ocean Data Analysis Project version 2 (GLODAPv2) - An internall consistent data product for the world ocean. *Earth System Science Data* **8**, 297-323 (2019).